OPEN ACCESS

University of BRISTOL

Psyrras, N., Kwon, O., Gerasimidis, S., & Sextos, A. (2019). Can a buried gas pipeline experience local buckling during earthquake ground shaking? *Soil Dynamics and Earthquake Engineering*, *116*, 511-529. https://doi.org/10.1016/j.soildyn.2018.10.027

Peer reviewed version

License (if available):
CC BY-NC-ND

Link to published version (if available):
10.1016/j.soildyn.2018.10.027

Link to publication record in Explore Bristol Research
PDF-document

This is the author accepted manuscript (AAM). The final published version (version of record) is available online via Elsevier at https://www.sciencedirect.com/science/article/pii/S026772611830616X . Please refer to any applicable terms of use of the publisher.

University of Bristol - Explore Bristol Research
General rights

This document is made available in accordance with publisher policies. Please cite only the published version using the reference above. Full terms of use are available:
http://www.bristol.ac.uk/red/research-policy/pure/user-guides/ebr-terms/

Can a buried gas pipeline experience local buckling during earthquake ground shaking?

N. Psyrras[1], O. Kwon[2], S. Gerasimidis[3] and A. Sextos[4]

Abstract. The damage potential of spatially variable seismic ground motion on buried pipelines has long been confirmed by field evidence, but it is still debatable whether transient seismic loads can be truly detrimental to the pipeline integrity. In the absence of systematic scrutiny of the effects of local site conditions on the seismic behaviour of such structures, this study presents a staged approach to numerically investigate the elastic-plastic buckling response of buried steel natural gas pipelines subject to transient differential ground motions arising from strong lateral site inhomogeneities. The first stage involves the study of 2D linear viscoelastic and equivalent-linear site response for the case of two sites and the resulting seismic demand in terms of longitudinal strains for input motions of various intensities and frequency content. The influence of key problem parameters is examined, and the most unfavourable relative ground deformation cases are identified. In the second stage of analysis, the critical in-plane ground displacement field is imposed monotonically on a near-field trench-like 3D continuum soil model encasing a long cylindrical shell model of the pipeline. Next, the performance of the buried pipeline is assessed under axial compression. The impedance contrast between the laterally inhomogeneous soil profiles is shown to govern the amplitude of induced elastic strains, which are maximized for low-frequency excitations. It is also demonstrated that peak axial strains along the pipeline considering equivalent-linear soil behaviour under strong earthquake motion can be as much as two orders of magnitude larger than their linear counterparts, as a result of the severe, spatially variable moduli degradation. It is finally shown that the seismic vibrations of certain inhomogeneous sites can produce appreciable axial stress concentration in the critically affected pipeline segment near the material discontinuity, enough to trigger coupled buckling modes in the plastic range. This behaviour is found to be controlled by pronounced axial force-bending moment interaction and is not accounted for in code-prescribed limit states.

Keywords. *soil-pipe interaction; natural gas; earthquake ground motion; inhomogeneous sites; wave propagation; local buckling; site response analysis*

[1] Ph.D Candidate, University of Bristol, UK
[2] Assoc. Professor, University of Toronto, Canada
[3] Assist. Professor, University of Massachusetts at Amherst, USA
[4] Professor, University of Bristol, UK & Aristotle University of Thessaloniki, Greece

1 Introduction

Safeguarding the operation of underground natural gas (NG) pipelines against earthquake hazards is imperative to life safety, the environment and the economy. Experience from past earthquakes shows that damage inflicted to buried NG pipelines can cause long service disruptions and unpredictably high socioeconomic losses. Globally, seismic risk is substantially high because many dense NG networks traverse large territories that are exposed to significant seismic hazard.

Pipelines of the transmission NG network system cross areas with diverse subsurface conditions to transport NG from wells to storage facilities, power plants and cities through distribution lines. Typically, these pipelines have large diameters exceeding 400 mm, high operating pressures in the range 3 ~ 15 MPa and are made from carbon steel with yield strength greater than 350 MPa. The individual pipe segments are joined together by welding to form a continuous system. Section design based on pressure load usually leads to radius-over-thickness ratios R/t of less than 50. The above properties dictate that for these structures, shell-mode instabilities may arise in the inelastic range of response under both axial and bending static loading [1]. Under a fairly low axial loading rate, such a shell will also buckle dynamically in an axisymmetric mode [2].

The earthquake response of long buried structures like NG pipelines is known to be controlled by transient and permanent (i.e., post-quake) ground strains rather than inertial effects. This is because the stiffness and mass of the embedded pipelines is negligible compared to that of the ground, hence they tend to deform following the imposed displacement of the soil. Determination of the input seismic load for structural analysis and design purposes thus must rely on methods that are able to reliably estimate the spatial variation along the pipeline axis and the peaks of ground strain in a given site. Solutions for the peak elastic strains in homogeneous soil solely due to the wave passage effect do exist [3,4], but local site effects, even though intuitively expected to cause significant strain amplification, have not been considered systematically neither in the literature nor in design codes in relation to pipeline seismic demand. Local site response is caused by gradients in soil properties (material inhomogeneity), surface topography (e.g., hills, ridges and canyons) and special geologic conditions, such as a soft surficial layer surrounded by stiff rock (valley-type) and cavities. Under optimally directed seismic excitation, the presence of any of the above in the vicinity of a buried pipeline can amplify the ground motion locally, alter its frequency characteristics and spatial profiles, prolong its duration and induce pronounced ground strains and curvatures (e.g., [5–9]) mainly close to the interface of different soil formations, which in turn can induce local pipeline deformation. As an example, a pipeline crossing the interface between soil strata that exhibit a sharp lateral change in stiffness will suffer principally from alternating axial compression-extension under direct seismic wave action, due to the different vibrational characteristics of the said strata, even if the pipeline fully conforms to the ground motion (i.e., no interaction). Since steel pipelines are buckling-sensitive structures for the reasons explained above, the compressive load resulting from the out-of-phase ground motion of adjacent soil media can, under

circumstances, exceed the critical buckling load of the shell, hence considerations on the buckling capacity of the pipeline need to be made. For the sake of argument, Figure 1 shows a simplified non-uniform site scenario along with different loading cases. The site consists of two horizontally adjacent soil deposits of different average wave speeds and is excited by vertically incident S-waves of varying polarization. Wave motion polarized in the pipeline direction induces axial strain in the pipeline near the boundary (marked with red in Figure 1a), while a parasitic vertical motion component forces the pipeline to bend in the vertical plane (deformed shape marked with a black line). Polarization in the transverse direction induces only bending in the horizontal plane near the boundary (Figure 1b). One immediately realizes that if the wave front is incident under angle,or the pipeline is aligned arbitrarily with respect to the soil particle motion (Figure 1c), multiple motion components will load the pipeline simultaneously.

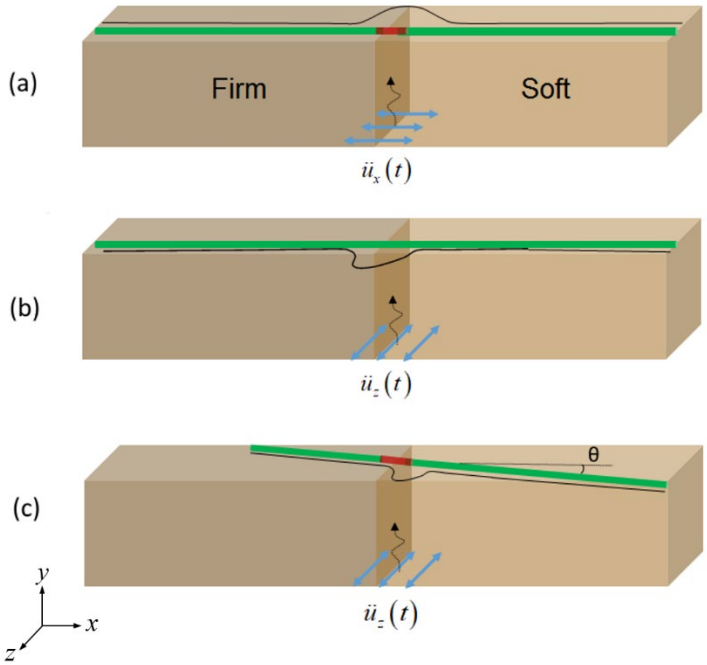

Figure 1. Schematic of buried NG pipeline crossing two laterally adjacent soil deposits of different stiffness. Three idealized loading scenarios and the associated deformed configurations of the pipeline are depicted: (a) a pipeline crossing the interface at right angles under *SV*-waves; (b) a pipeline crossing the interface at right angles under *SH*-wave excitation; (c) a pipeline crossing the interface at an arbitrary angle under *SH*-waves. Marked with red are the axial straining zones, while the black lines indicate qualitatively the flexural deformation shapes of the pipe.

Field evidence supports the above considerations. Most of the pipeline damage reported to date is due to permanent ground deformation [10,11], but there is also indisputable evidence that wave propagation can be damaging [12–18]. Local buckling failures in steel pipelines have been systematically reported [13,19]. In such cases, the highly localized curvatures associated with local buckling modes can cause wall tearing and content leakage or accelerate fatigue damage if not diagnosed in time. Therefore, every effort should be taken in the design phase to minimize these risks.

The effects of the spatial variation of ground motion (SVGM) on the seismic behavior of buried pipelines have largely been addressed from three main perspectives in terms of seismic input: travelling seismic waves in homogeneous sites, loss of wave coherency in inhomogeneous sites and 2D/3D local site response. The majority of published research has focused on the first; incoherency and local site effects have received less attention comparatively. Hindy and Novak [20] studied analytically elastic pipelines both in homogeneous sites and in sites consisting of two different media in the horizontal sense. It was found that for body waves propagating along the pipeline, the peak axial and bending stresses occur near the boundary of the two media and are larger than the ones in the homogeneous case. Predictions also revealed that bending stresses due to S-waves are much smaller than the axial stresses due to P-waves. Later, Nishio *et al.* [21,22] conducted laboratory tests of buried pipelines in valley and cut-and-fill settings subject to horizontal base excitation. Analytical methods were used to study the strain response of buried pipelines laid through dipping soil layers [23,24], cut-and-fill embankments [25], riverbeds [26] and multiple soil media [27].

Buried pipelines under statistically incoherent seismic motions have also been a subject of scrutiny. Zerva *et al.* [28] and Zerva [29] examined the axial and transverse elastic response of segmented and continuous pipelines to differential ground motion using random vibration analysis on analytical pipeline models, where the seismic input was described by the stochastic properties of ground motions recorded at the dense SMART-1 array. Axial strains were observed to be the principal source of pipeline deformation over bending strains; the magnitudes of these (average) strains were estimated however at least an order below usual steel yield limits. It was also shown that the influence of the incoherence parameter on the pipeline response is critical.

From the viewpoint of structural stability, elastic and inelastic buckling and collapse of standalone cylindrical shells is a well-established topic in the literature. On the other hand, buckling of shallow-buried cylindrical shells, which involves additional motion constraints, is not as mature a topic. Chen *et al.* [30] used shell stability formulations to study the elastic static axial buckling of a buried pipeline. Lee *et al.* [2] developed an elastic-plastic cylindrical shell formulation for a buried pressurized pipeline in a homogeneous elastic medium to check for the stability of the dynamic equilibrium of the pipe shell. In this treatment, axial soil-pipe interaction was ignored, and a lateral soil restraint was assumed in the form of distributed elastic radial springs. The solutions derived showed that the critical axisymmetric buckling stress and strain of the pipeline under dynamic conditions are essentially the same as under static conditions. Yun and Kyriakides [31] examined in detail the conditions under which a buried pipeline loaded in uniform compression may bifurcate plastically into a beam or an axisymmetric shell mode, as well as the possibility of interaction between the two. Lateral soil confinement was considered in the radial sense through a nonlinear spring model. Their sensitivity analyses show qualitatively that combination of conditions such as large pipe diameter, large R/t ratio and deep soil cover favour shell-mode buckling, and that the buckling stress of the pipeline is highly sensitive to the amplitude of the initial imperfections.

Acknowledging that studying the buckling behaviour of high-pressure steel pipelines embedded in seismic soil environments with material inhomogeneities is rather challenging and that certain assumptions are often indispensable, it is pointed out that previous research on the topic has either focused on (i) the beam-type response of the pipeline using simple beam-on-springs models, thus ignoring shell buckling phenomena, or (ii) the spatially variable seismic ground demand considering mainly the wave passage effect in elastic homogeneous soils, or (iii) the determination of the buckling capacity of buried pipelines using simplified interaction models but ignoring the true level of pipeline demand induced by wave propagation. Investigations of the seismic demand of the pipeline shell generated by the local site seismic response considering nonlinear soil and pipeline constitutive behaviour, large-deformation kinematics and SPI effects are absent from the literature. Psyrras and Sextos [32] present a comprehensive review of all above aspects. It remains to be clarified whether and under what conditions wave propagation-induced pipe strains are likely to develop that can lead to such critical limit states as shell-mode buckling.

In this study, we break down and analyze the problem efficiently in two successive phases, employing as few simplifications as possible. Recognizing that contact effects are critical to the axial response of a buried pipeline [33], we develop refined finite element models of a certain class of graded geologic media and the cylindrical shell pipeline running through them, in order to:

- predict the range of peak magnitudes and the spatial distributions of the longitudinal ground strains along the pipe developing under low- and high-intensity motions, respectively, with the aim to highlight the most critical cases;
- illustrate the sensitivity of the induced seismic ground strains to various involved parameters;
- evaluate the pipeline demand resulting from the imposed critical soil displacement fields and analyse the interaction effects at the soil-pipeline interface;
- ultimately explore the possibility of buckling collapse in high-pressure steel NG pipelines laid through such sites, study its characteristics and showcase the circumstances that favour its occurrence.

The structure of this text is as follows. First, the analysis methodology is outlined and the associated assumptions and limitations are discussed. Next, each analysis step is presented with details of the models developed, and results of the analyses undertaken are illustrated. Finally, the most important findings are summarized and implications are discussed.

2 Methodology

The emphasis in this investigation is placed on the failure mechanism that is most likely to occur in a pipeline under the given seismic excitation. This is expected to be shell-mode buckling due to axial compression resulting from large differential axial displacements of the surrounding soil in a confined region containing the inhomogeneity border. It is well known that the response of constrained and

unconstrained shells in compression is generally governed by buckling. Previous research and field evidence have demonstrated that, under transient ground deformation, buried steel-welded NG pipelines are not anticipated to experience tensile rupture, and also that other possible failure modes, such as beam-mode buckling and section ovalization, are not detrimental to their integrity and operability [32]. However, simultaneous appearance and interaction between different mechanisms cannot be ignored. The progression of the simulation phases described next is founded on the above arguments.

A large-scale 3D finite element simulation of the dynamic response of the interacting soil-pipe system would ideally be the most rigorous approach one could follow; however, it is hindered by the associated difficulty in reliably interpreting the results, the extreme computational load, and the high level of uncertainty involved in the model parameters. Besides, it has been observed that considering 3D wave effects in the site response does not always offer increased fidelity over a 2D or even 1D analysis [34]. On the other hand, the commonly used 1D site response models had to be discarded in the first place as an option because they cannot capture the gradient of ground motion in a dimension other than depth.

It is also long recognized that classical –inertial and kinematic– soil-structure interaction (SSI) effects are rather unimportant in a dynamic soil-pipe interaction (SPI) problem [35–37]. This observation allows decoupling the problem and treating it in two successive stages at reduced computational effort compared to a direct 3D dynamic SPI analysis. Therefore, the whole SPI problem degenerates into a continuous contact problem governed by the soil motion, where the interface behaviour can be represented either rigorously using explicit contact elements or approximately with macro-elements.

A sketch of the proposed sub-structuring procedure is given in Figure 2 where only fundamental aspects are shown. The procedure follows closely Ando *et al.*[25], Papadopoulos *et al.* [38] and Psyrras *et al.* [39]. As a disclaimer, it is stressed that the methodology presented is not aimed to replace established analysis techniques or engineering judgment in everyday design projects.

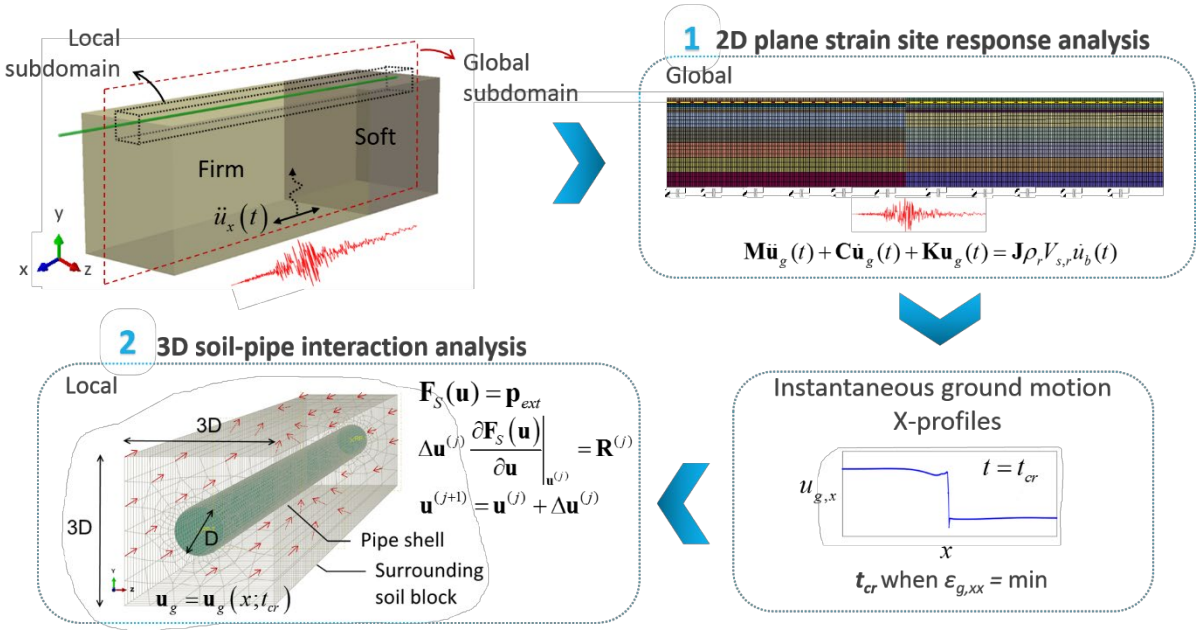

$\mathbf{M},\mathbf{C},\mathbf{K}$ = mass, viscous damping and stiffness matrices of the soil domain

$\ddot{\mathbf{u}}_g(t),\dot{\mathbf{u}}_g(t),\mathbf{u}_g(t)$ = absolute acceleration, velocity and displacement nodal point vectors

$\rho_r, V_{s,r}$ = mass density and elastic s-wave velocity of bedrock

$\mathbf{J}, \dot{u}_b(t)$ = influence vector and bedrock velocity time history

$\mathbf{F}_S(\mathbf{u})$ = vector of resisting forces

$\mathbf{p}_{ext}$ = vector of external forces

$\mathbf{u}^{(j)}, \mathbf{u}^{(j+1)}$ = estimate of nodal displacements after j and $j+1$ iterations

$\Delta\mathbf{u}^{(j)}$ = change of displacements within $j+1$ iteration

$\mathbf{R}^{(j)}$ = residual force vector within $j+1$ iteration

Figure 2. Problem sub-structuring: (1) 2D FE ground response analysis to earthquake and extraction of the critical deformation profile of the soil at pipeline depth; (2) application of this profile as an incremental load on the 3D soil body of the local soil-pipeline FE assembly to evaluate the pipeline demand; the system of nonlinear algebraic equations is solved using any appropriate solution algorithm (standard Newton-Raphson scheme shown here).

Stage 1: Equivalent linear site response

Stage (1) involves prediction of the transient ground response of deep soil sites overlying elastic rock to plane shear waves of arbitrary incidence. More specifically, the goal is to predict the peak values and spatial distributions of the longitudinal ground strains. Given that the direction of the wavefront relative to the pipeline alignment can be arbitrary, it seems reasonable to study the case leading to the most critical pipeline deformation, that is, where particle motion is fully in-plane with the pipeline axis (Figure 3). Shear waves are considered because they are known to carry most of the elastic energy. Moreover, it is well-established that, unless highly plastic, soils exhibit nonlinearity in their shear stress-strain response even for small cyclic strains [40,41]. This behavior should be captured in our analyses because a substantial drop in stiffness may very well relate to higher potential for normal straining.

Idealized sites characterized by inhomogeneity in soil properties along both orthogonal axes are considered as being representative of real-world, near-surface conditions. 2D seismic site response analyses are performed in the time domain under plane-strain conditions, assuming viscoelastic or strain-compatible soil material properties. Simple pulses and real earthquake records are used as input excitation. Parameter variation generates a set of analysis cases for each site scenario and the ground response histories are evaluated towards the identification of the most unfavourable spatial profiles, the criterion being the peak longitudinal compressive ground strain ($\varepsilon_{g,c}^{max}$). This parametric study allows to highlight the influence of different problem variables on $\varepsilon_{g,c}^{max}$. Details on the site response models are provided in Section 3.

Stage 2: Soil-pipe interaction considering interface contact and steel buckling

In stage (2), a detailed numerical model is developed consisting of a long portion of the pipeline and an extended trench. The length of the model along the pipeline axis matches that of the 2D site response model. The absence of strong SSI effects, the assumption of in-plane ground motion, and the typically shallow embedment depth of the pipeline allows us to truncate only a surficial block from the semi-

infinite 3D soil domain, starting from a few meters below the ditch line and reaching up to the surface. The pipeline is assumed to run parallel to the surface of the 2D ground response models. The out-of-plane width with respect to the primary axes of the plane-strain model is selected large enough to allow development of in-situ soil pressures and out-of-plane pipe deformation. A thin circular cylindrical shell model based on Koiter-Sanders theory is created to represent the pipeline, while the trench soil is simulated with 3D continuum elements. In this fashion, localized buckling modes can develop in the pipe under axial compression and also the initial stress state and deformation due to gravity and pipe internal pressure are calculated prior to the application of the seismic load. Contact between the soil and the pipe is modelled rigorously by means of contact elements able to simulate surface-to-surface slippage, separation, and the coupling between them explicitly. In this way, the load transfer mechanism from soil to pipe is effectively captured. The originally dynamic problem is now reduced to a quasi-static one, since pipeline inertia is negligible compared to that of the soil.

All major energy dissipation mechanisms need also to be at least indirectly considered. In a SPI problem, material damping is predominantly attributed to soil action. In our approach, soil material damping has already been included in stage (1), both the hysteretic (indirectly) and the linear viscous forms of it. Radiation damping has also been considered in stage (1) by means of absorbing boundaries of the ground response models. Another form of energy dissipation is due to nonlinear contact at the soil-pipe interface, which is explicitly modelled in stage (2).

Assumptions and limitations

With the analysis approach described, 2D wave effects are captured but 3D ones are inevitably disregarded. The fundamental assumption is that inertial SPI (i.e., wave emitted by the vibration of the pipe) and kinematic SPI (i.e., ground motion modification due to the stiffness contrast between the soil and the pipe) can be ignored with acceptable loss of accuracy. The error introduced by this approximation on the whole is not easily quantifiable in this study; a prohibitively costly 3D dynamic SPI analysis would be required to compute a reference system response, which would essentially cancel the merits of the proposed approach. However, a simple way to quantitively argue about the error related to the inertial interaction effect is to consider the ratio of the weight of the pipe to the weight of the soil it replaces $w_p / w_s = 2\left(\rho_p / \rho_s\right)\left(t/R\right)$. For typical NG steel pipelines and soils, this ratio takes values in the range 0.16 ~ 0.52, which implies a 'negative' inertial interaction. As regards kinematic interaction, it is certain that the influence of the pipe stiffness on the free-field motion around the pipe is negligible. This has been concluded upon examination of free-field acceleration response histories computed from 2D site response analysis with and without the embedded pipe, not presented here.

Moreover, soil deformation occurs only in the plane defined by the pipeline longitudinal axis and the vertical. Soil nonlinearity is only approximately accounted for since neither yielding nor hardening effects nor permanent deformation can be described through the equivalent-linear analyses undertaken. In stage (1), total stresses are computed assuming dry cohesionless soils (drained conditions in the

absence of groundwater head). For cases where soil nonlinearity is expected to be very pronounced (extremely high-intensity motions, liquefiable soils etc.), equivalent-linear analysis procedures cease to be reliable and more advanced nonlinear models have to be employed [42]. Furthermore, we can neither track the over-time evolution of pipeline stresses and deformations, nor capture the influence of time-dependent phenomena such as fatigue and steel strength and stiffness degradation due to cyclic loading. The bifurcation stress and strain of the pipeline can be considered reliable only to the degree that the assumption of equivalence between the static and dynamic buckling strength holds true.

3 Seismic ground response analysis

3.1 Scenario selection

Because we aim for a general treatment of the problem to illuminate its governing features, we do not limit the scope of this study to real sites, rather we opt for a scenario-based approach. To this end, two generic site scenarios are considered: (i) a simple site consisting of two laterally adjacent soil deposits of dissimilar shear wave velocities, their boundary being vertical (*scenario 1*), and (ii) a symmetric trapezoidal sediment-filled valley (*scenario 2*). The two sites are illustrated in Figure 3 (left) with their 2D cross section sketched in Figure 3 (right). Particle motion is constrained in two dimensions as the half-plane is swept only by upward travelling, vertically polarized plane shear (*SV*) waves. The seismic motions are assumed to be fully correlated at the bedrock level, except the phase velocity effect in case of non-vertical incidence. To examine the strain response to weak input motions (PGA<0.05g), plane strain, linear viscoelastic site response analyses are conducted with variation of key problem parameters. For stronger ground motion, able to trigger nonlinear soil response, an iterative scheme is employed to achieve strain-compatible soil properties according to published nonlinear curves.

The vertical boundary in scenario 1 is assumed to extend out-of-plane to infinity and the out-of-plane valley dimension in scenario 2 is assumed to be large enough, which is a common trait of valleys formed around rivers. On these grounds, the assumed plane-strain conditions can be warranted. Both scenarios are assumed to be flat-surface sites, hence no topography effects are considered. The valley is classified as shallow and wide according to Kramer [43]. The different model cases are identified using the conventions 'S_iL_j' and 'S_iNL_j', where S denotes the scenario, L/NL stands for linear/nonlinear soil behavior and i and j are substituted by the scenario and the case ID, respectively.

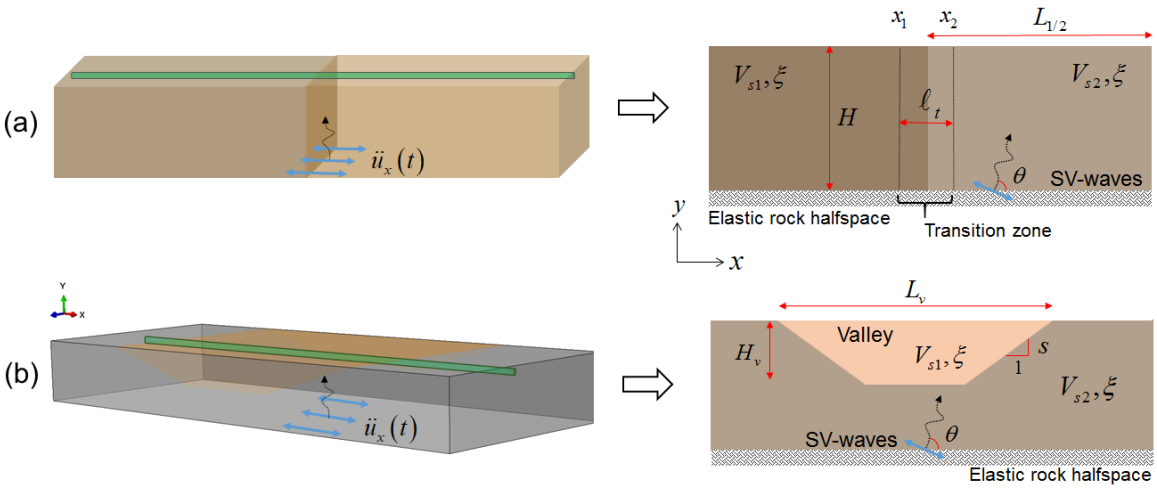

Figure 3. Idealization of the two scenarios under consideration (left) and identification of the important problem parameters (right) for linear elastic conditions: (a) scenario 1 and (b) scenario 2.

3.2 Site characterization, stratigraphy and soil nonlinearity

3.2.1 Linear elastic models

First, ground response analyses assuming linearly viscoelastic soil were conducted to investigate the effect of weak bedrock input motion on the surface amplification patterns, wavefield scattering and, most importantly, the induced axial ground strains at pipeline depth. As shown also in Figure 3, the different soil deposits in both scenarios are assumed vertically homogeneous. In reality, soils usually exhibit increasing stiffness with depth, but for the sake of simplicity and ease of interpretation, the elastic deposits examined in this study display constant S-wave velocity profiles $V_{s,1}$ and $V_{s,2}$, respectively. Preliminary results from incremental equivalent-linear analyses revealed that a bedrock *PGA* of roughly 0.05g bounds the ground response in the linear regime from above. To this end, all input acceleration time histories were scaled to this value.

Figure 3 (right column) identifies the governing geometric and material parameters of the idealized physical model. Parameters that were initially left to vary for scenario 1 sites are the S-wave velocity of the left deposit $V_{s,1}$, the depth to bedrock H, the stiffness transition zone length ℓ_t, the small-strain critical damping ratio ξ and the wave incidence angle θ. An invariant $V_{s,2} = 100$ m/sec is assumed and a uniform mass density of $1.7\,Mg/m^3$ is assigned to both deposits to reduce the number of parameters. Normalized quantities were introduced as follows: the dimensionless frequency $a_0 = \omega / \omega_{o,2} = 4 f_o H / V_{s,2}$, the site impedance ratio which reduces to the velocity contrast $V_{s,1}/V_{s,2}$, and the dimensionless transition zone length ℓ_t / H. $L_{1/2}$ is the half-length of the domain and is set equal to 250m. Note that $L_{1/2}$ is not really a parameter of the physical problem; it appears only in the numerical one because truncation of the domain sidewise is necessary to render it finite. In the absence of known characteristic patterns in nature, a linear lateral variation of the soil stiffness was assumed along a

transition zone and its length $\ell_t = x_2 - x_1$ was varied. The variation of shear modulus with the horizontal position coordinate is expressed as:

$$G(x) = \begin{cases} G_1, & x \le x_1 \\ G_1 + \dfrac{G_2 - G_1}{\ell_t} x, & x_1 \le x \le x_2 \\ G_2, & x \ge x_2 \end{cases} \quad (1)$$

For scenario 2, the dimensionless frequency takes the form $a_0 = \omega / \omega_{o,1} = 4fH_v / V_{s,1}$, implying reference to a 1D soil column with properties equivalent to the valley soil, and the slope *s* of the inclined boundary is additionally introduced in the problem. The mass densities of the valley soil and the surrounding rock are $1.7\,\mathrm{Mg/m^3}$ and $2\,\mathrm{Mg/m^3}$ respectively. The valley width at the surface and its depth are $L_v = 300$ m and $H_v = 30$ m, respectively, giving a depth-to-width ratio of 0.1. The total domain length is again 500 m. Table 1 contains the parameter values examined in this study. FE code Abaqus [44] supplemented by OpenSees [45] were employed to develop and solve these models. Abaqus was the main solver where advantage was taken of the USDFLD user-subroutine to introduce the desired lateral stiffness gradients in the soil body. OpenSees was used to implement the so-called 'free-field' boundaries at the lateral sides of the 2D model, as described in Section 3.3.

Table 1. Range of values considered for the dimensionless parameters of the two scenarios

Scenario 1		Scenario 2	
a_0	0.6, 1.2, 2.4, 6, 12	a_0	0.43, 0.86, 1.7, 3.43, 4.3, 8.6
$V_{s,1} / V_{s,2}$	0.7, 1.4, 2, 4	$V_{s,1} / V_{s,2}$	0.0875, 0.175, 0.35
θ	0°, 10°, 20°, 30°	θ	0°, 10°, 20°
ℓ_t / H	0.33, 1, 1.66	s	30%, 60%
ξ	2% , 5%	ξ	2%, 5%

Typical values for the elastic and mass properties of the bedrock are considered in all analysis cases, namely $\rho_r = 2.4$ Mg/m^3 and $V_{s,r} = 1000$ m/sec, the latter representing a rather normally stiff rock. The Poisson ratio for all soils is taken constant $v = 1/3$.

3.2.2 Equivalent-linear models

To avoid unnecessary workload in this section, we discard from the list of the examined parameters those ones that are shown later in Section 3.5.1 to have minimal influence on the axial strain response. These are the transition zone length and the wave incidence angle for scenario 1 and the wave incidence angle for scenario 2.

The variation of soil shear moduli and critical damping ratio with cyclic shear strain γ_c is fundamentally dependent on the in-situ confining pressure, an effect reflected in the state-of-the-art soil moduli degradation and damping curves. In light of this, we introduced further variation of the small-

strain shear modulus $G_{\max}$ with depth determined by the Seed and Idriss [46] empirical formula for sands (Eq. (2)):

$$G_{\max} = 220 K_{2,\max} (\sigma'_m)^{0.5} \quad (2)$$

$$V_s = \sqrt{G_{\max} / \rho} \quad (3)$$

where σ'_m is the mean effective confining stress and $K_{2,\max}$ a constant found in relevant tables [43] as a function of the relative density D_r of the soil. Therefore, a different ρ is specified for each soil deposit of scenario 1, with its value providing a density characterization (loose, medium or dense) according to Table 2. Three different vertical wave speed profiles are generated based on this methodology and three different analysis cases can be drawn from their combinations, all other factors being constant. The continuous and discretized V_s profiles for one of these cases are plotted in Figure 4a. For scenario 2, only the valley geomaterial is assumed equivalent-linear and different mass densities ρ_V are assigned to it to generate the vertical V_s profile. The surrounding stiff soil is assumed to respond linearly and to possess uniform stiffness.

Table 2. Relationships between mass density, relative density, $K_{2,max}$ parameter and soil characterization

ρ (Mg/m^3)	D_r (%)	$K_{2,\max}$ (-)	Characterization
1.4	30	30	Loose
1.65	52.5	48	Medium
2	90	70	Fine

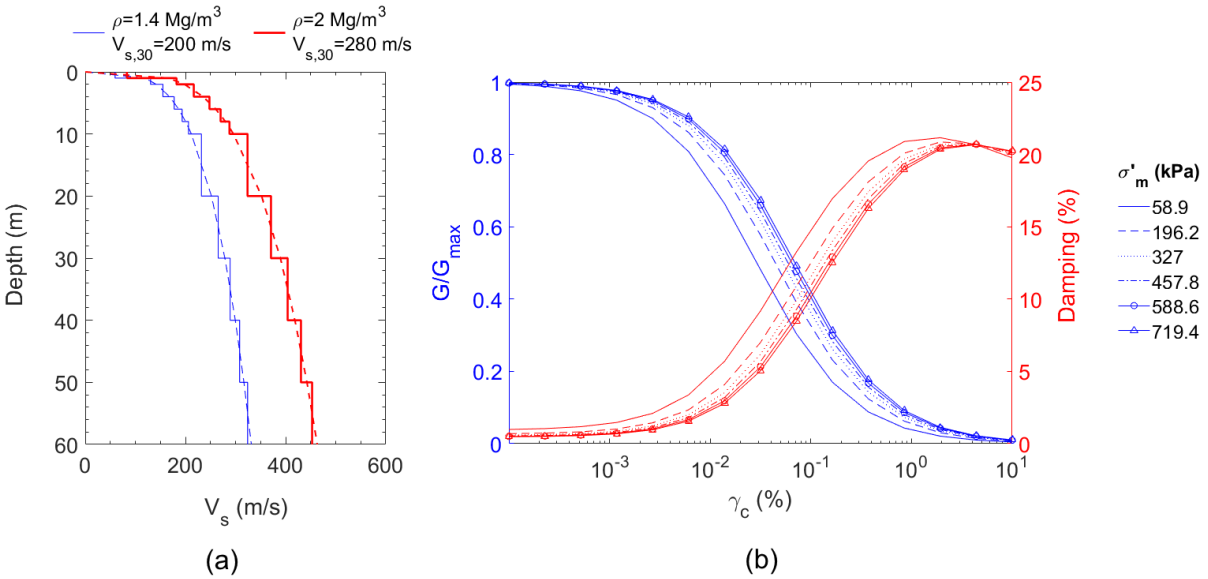

Figure 4. (a) Vertical V_s profiles generated for the two deposits of case S1NL1; (b) moduli degradation and damping curves [47] calculated for the different discrete layers comprising one soil deposit of case S1NL3 (an averaged σ'_m is taken every 10m depth).

Shear moduli and damping ratios for each soil element are independently adjusted at the end of each linear dynamic analysis to match strain-compatible values as given by *G*-γ-*D* curves. The strain measure that is used for this iterative process is 65% of the maximum shear strain, which for plane-strain conditions assumes the following form:

$$\gamma_{\max} = \sqrt{\left(\varepsilon_{xx} - \varepsilon_{yy}\right)^2 + \gamma_{xy}^2} \tag{4}$$

where γ_{xy} represents the cartesian engineering shear strain and ε_{ii} are the cartesian normal strain components. The computer code QUAD4M [48] for 2D seismic site response analysis is used for this purpose. From the published soil curve sets examined [46,47,49,50], the Darendeli model was adopted because it is analytical, pressure-dependent, robust and generally provides conservative results. To represent the depth-variation of $G_{\max}$ in a discrete manner, each deposit is subdivided into sub-layers, each with a maximum depth of 10 m. An averaged σ'_m is then computed for each sub-layer and a different *G*-γ-*D* curve is assigned to it, as illustrated in Figure 4b.

3.3 Domain discretization, boundary conditions and seismic excitation

Element discretization in the vertical sense has so been performed as to allow adequate resolution of frequencies up to 15 Hz in the range of wave velocities used in this study. For this purpose, it was ensured that at least 8 finite elements subdivide each wave length. Newmark's unconditionally stable explicit time-stepping algorithm with $a = 0.25$ and $b = 0.5$ for linear dynamics was used to integrate the equations of motion in time, therefore no further constraint was imposed on the size of the finite elements. Linear quadrilateral and triangular elements were used. The lateral truncation of the medium has been carried out in a way to ensure convergence of the axial strain distribution at the surface. Indicative meshes for both scenarios are pictured in Figure 5.

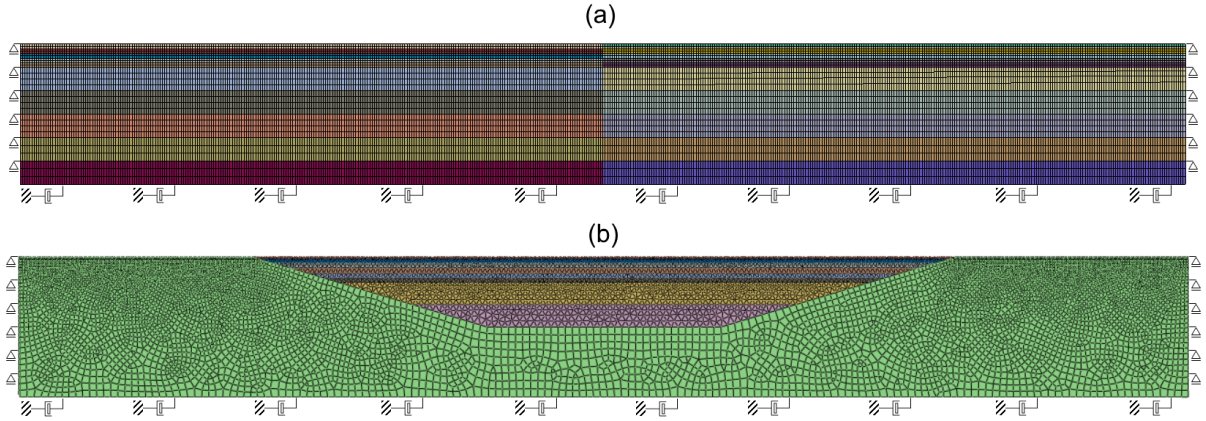

Figure 5. FE discretization and soil layering for typical equivalent-linear site cases of (a) scenario 1 and (b) scenario 2; visible is the progressive reduction in element size towards the softer material at the surface.

Standard local absorbing boundaries [51] in the form of normal and tangential viscous dashpots were implemented at the base of the linear and equivalent-linear models to represent the radiation of outgoing

seismic waves. In the linear models, 'free-field' boundaries were applied at the lateral sides to represent the far-field response of the laterally infinite medium. An auxiliary 1D wave propagation model matching the geometry, mesh and properties of the lateral boundaries of the Abaqus 2D model is solved in OpenSees and the velocity response histories of its nodes are imposed as boundary conditions on the corresponding end nodes of the dashpots of the Abaqus 2D model. This was not possible to implement in QUAD4M and for this reason the conditions imposed on the lateral boundaries of the equivalent-linear models were those of the standard 1D soil column (shear beam mode). However, the length of the domain is large enough to allow effective dissipation of spurious wave reflections, which is expedited by the increased material damping ratios due to the equivalent-linear response.

To gain understanding into the frequency-dependency of wave scattering and induced axial strains, we excite the linear elastic models with pulse-like waveforms characterized by a narrow frequency bandwidth and a clearly dominant frequency. For this purpose, Ricker wavelets [52] are used to represent acceleration pulses with bedrock amplitude of $a = 0.05$ g, described by Eq. (5):

$$\ddot{u}(t) = a \cdot \left[1 - 2\pi^2 f_o^2 \left(t - t_o\right)^2\right] \cdot e^{-\pi^2 f_o^2 (t - t_o)^2} \tag{5}$$

where f_o is the predominant frequency and t_o the time instant of the peak of the pulse. The same wavelets are used for equivalent-linear analysis but scaled to 0.2g (Figure 6). Although in strict terms a pulse-like excitation (near-source sites) and a plane wave front (far-source sites) might be contradicting assumptions, they are both adopted in this study to simplify the models and facilitate interpretation of results. Furthermore, three far-source ($d_w > 10$ km) strong earthquake records of varying mean periods (T_m) calculated as proposed in Ref. [53] were selected as input to the equivalent-linear models (Figure 7), with properties presented in Table 3. Tables 4 and 5 contain all equivalent-linear analysis cases run for scenario 1 and 2, respectively, where the site impedance ratio is the ratio of the product $\rho \cdot V_{s,30}$ of the two adjacent deposits.

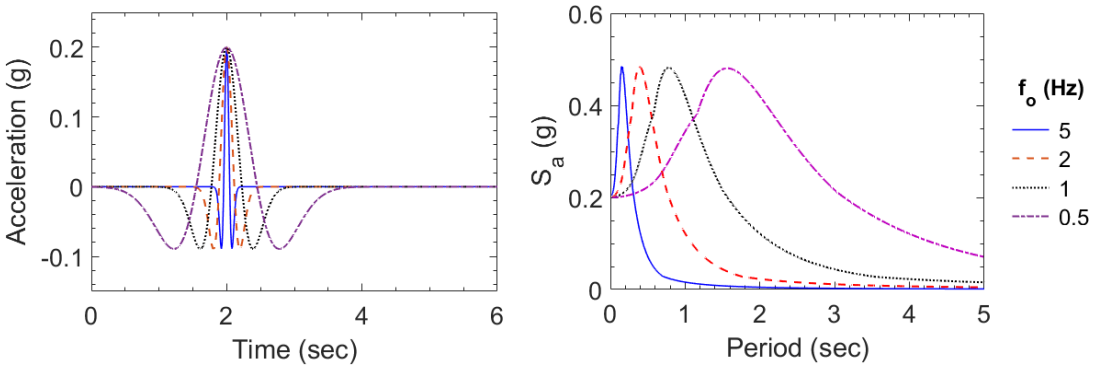

Figure 6. Acceleration time-histories of three Ricker wavelets with varying predominant frequencies (left) and their 5% damped elastic spectra (right).

Table 3. List of real outcrop earthquake records used as input motions

ID	Event	Magnitude, M_w	PGA (g)	Mean period, T_m (sec)	Predominant period, T_p (sec)
EQ1	Imperial Valley (1979)	6.4	0.32	0.40	0.26
EQ2	Chi-Chi (1999)	7.7	0.18	0.97	0.54
EQ3	Kocaeli (1999)	7.6	0.35	1.25	0.31

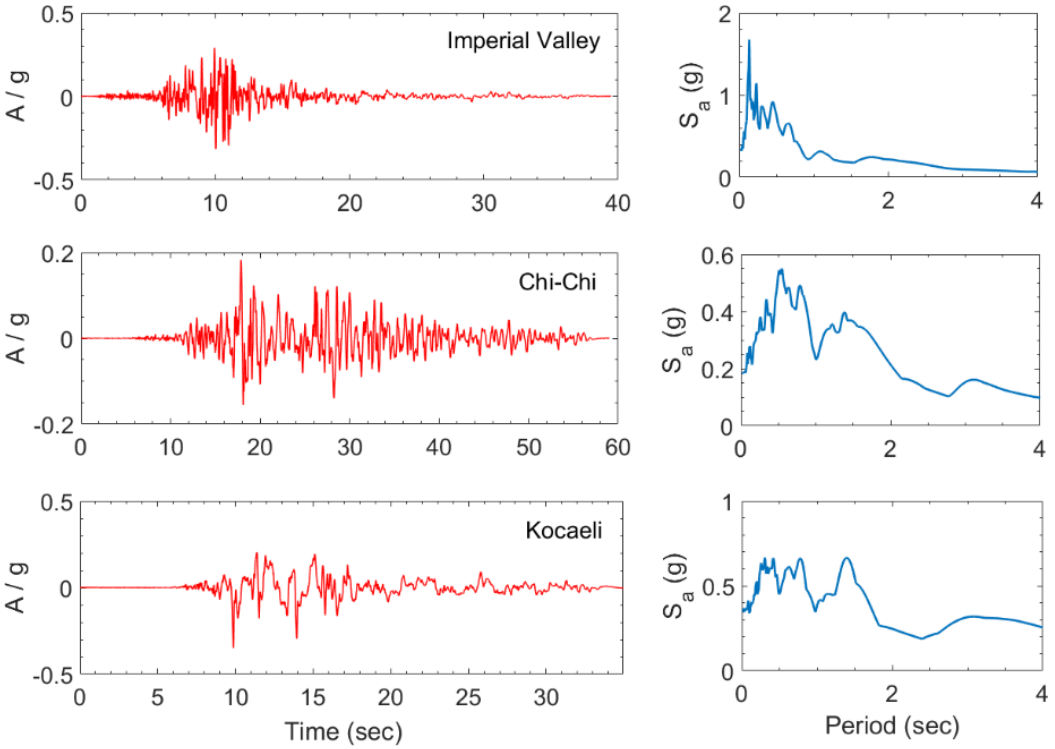

Figure 7. Acceleration time-histories (left) and the corresponding 5% damped elastic spectra of the earthquake records used as bedrock input motions (right).

Table 4. List of model parameters of equivalent-linear analysis cases for scenario 1

Case ID	ρ_1 **(Mg/m³)**	ρ_2 **(Mg/m³)**	**Depth-to-bedrock (m)**	**Site impedance ratio**	**Input motion**
S1NL0 (ref.)	2.00	1.4	60	0.5	EQ1
S1NL1	2.00	1.65	60	0.7	EQ1
S1NL2	1.65	1.4	60	0.7	EQ1
S1NL3	2.00	1.4	30	0.5	EQ1
S1NL4	2.00	1.4	90	0.5	EQ1
S1NL5	2.00	1.4	60	0.5	R05(*)
S1NL6	2.00	1.4	60	0.5	R1
S1NL7	2.00	1.4	60	0.5	R3
S1NL8	2.00	1.4	60	0.5	EQ2
S1NL9	2.00	1.4	60	0.5	EQ3

(*) **R*x*: Ricker wavelet with frequency of *x* Hz**

Table 5. List of model parameters of equivalent-linear analysis cases for scenario 2

Case ID	ρ_v (Mg/m^3)	$V_{s,r}$ (m/sec)	Dipping angle (%)	Site impedance ratio	Input motion
S2NL0 (ref.)	1.4	400	30	0.5	EQ1
S2NL1	1.65	400	30	0.6	EQ1
S2NL2	2	400	30	0.7	EQ1
S2NL3	1.4	400	60	0.5	EQ1
S2NL4	1.4	800	30	0.35	EQ1
S2NL5	1.4	400	30	0.5	R05(*)
S2NL6	1.4	400	30	0.5	R1
S2NL7	1.4	400	30	0.5	R3
S2NL8	1.4	400	30	0.5	EQ2
S2NL9	1.4	400	30	0.5	EQ3

(*) R*x*: Ricker wavelet with frequency of *x* Hz

Small-strain damping is assumed to be of the Rayleigh type, where the mass- and stiffness proportional coefficients are calculated by matching the Rayleigh damping ratio ξ with the target linear hysteretic critical damping ratio at two significant frequencies: the fundamental free vibration frequency ω_o and $n\omega_o$, where n is the smallest odd integer bigger than ω_p/ω_o, ω_p being the predominant frequency of the input motion. Its value is taken constant 2%.

3.4 Model verification

In the absence of exact elastic or viscoelastic wave solutions for the types of domains treated here, the accuracy of the predictions provided by the 2D soil models is checked against 1D closed-form theoretical solutions in the frequency domain, only for the case of laterally uniform soil layers. A typical layered soil over elastic half-space with equivalent-linear properties described by the Seed and Idriss curves is modelled in DeepSoil [54] under 1D site response conditions and is then subjected to the Northridge (1994), CDMG station, earthquake record. The computed response is compared to the one obtained by the 2D site analog modelled in QUAD4M. The surface-to-bedrock transfer functions are shown in Figure 8. A satisfactory match is observed between the 1D and the 2D equivalent-linear representations, with the 2D model over-predicting the response by a peak 27% at the intermediate frequencies. The marked discrepancies at certain frequency ranges can be attributed to underdamping and overdamping of the 2D response due to the frequency-dependent nature of the Rayleigh damping formulation.

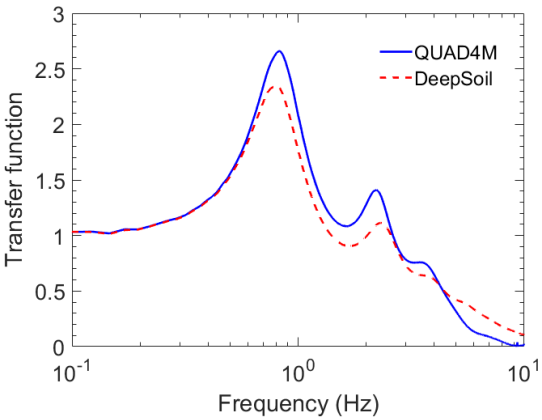

Figure 8. Comparison of surface-to-bedrock motion amplification factors for 1D and 2D equivalent-linear site response.

3.5 Free-field response results

3.5.1 Linear viscoelastic response (weak input motion)

Due to the breadth of the produced output, results are presented in various forms to highlight different features of interest. The different response quantities are plotted against the normalized horizontal coordinate $x/L_{1/2}$. Figure 9 shows envelopes of the peak tensile and compressive axial strains at different surface positions for some typical scenario 1 cases. Figure 10 shows the same but for scenario 2 cases. As expected for scenario 1, all cases exhibit peak strains in the softer of the two soils, in close proximity to their vertical border. Tensile strains are almost exact reflections of the compressive ones. Some large strain magnitudes are observed at the lateral boundaries and this might indicate the influence of the boundary conditions. With regard to scenario 2, peak surface strains are detected over the wedge toes; strain values tend to zero in rock and in the middle where the horizontal displacements attain their peaks due to the constructive interference of *R*-waves. In both scenarios, strains are larger for larger velocity contrast and smaller a_0. It should be made clear that the strains plotted are not concurrent.

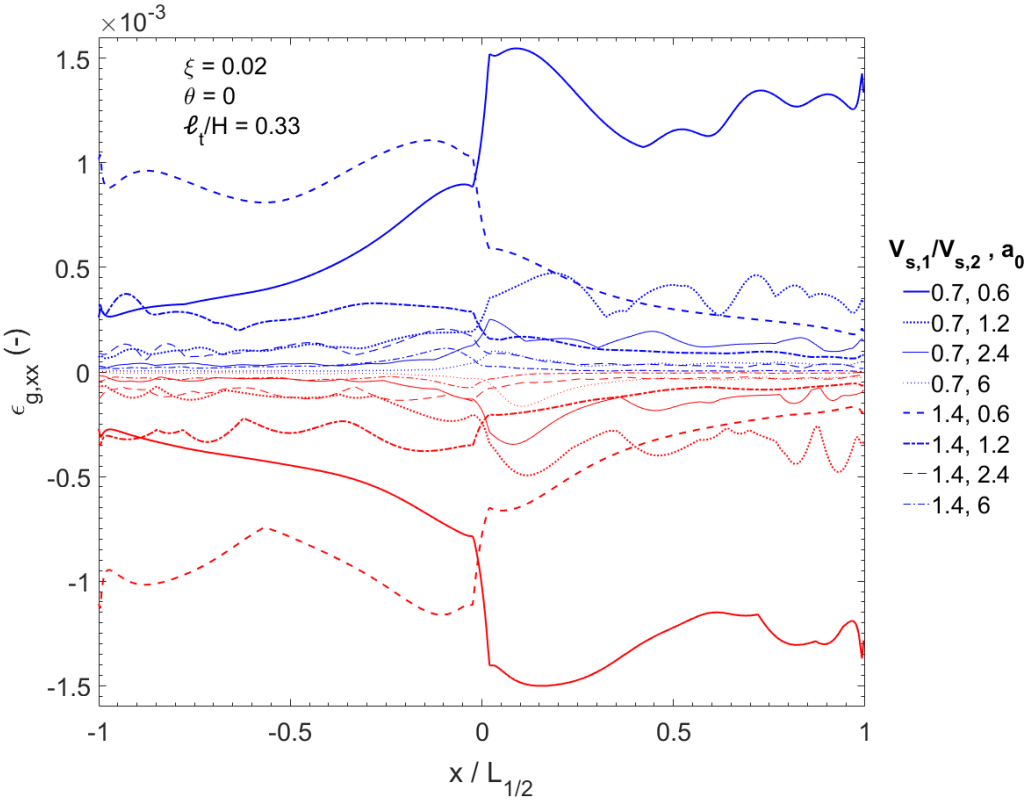

Figure 9. Envelopes of peak tensile (positive) and compressive (negative) axial ground strains along the surface for different scenario 1 cases.

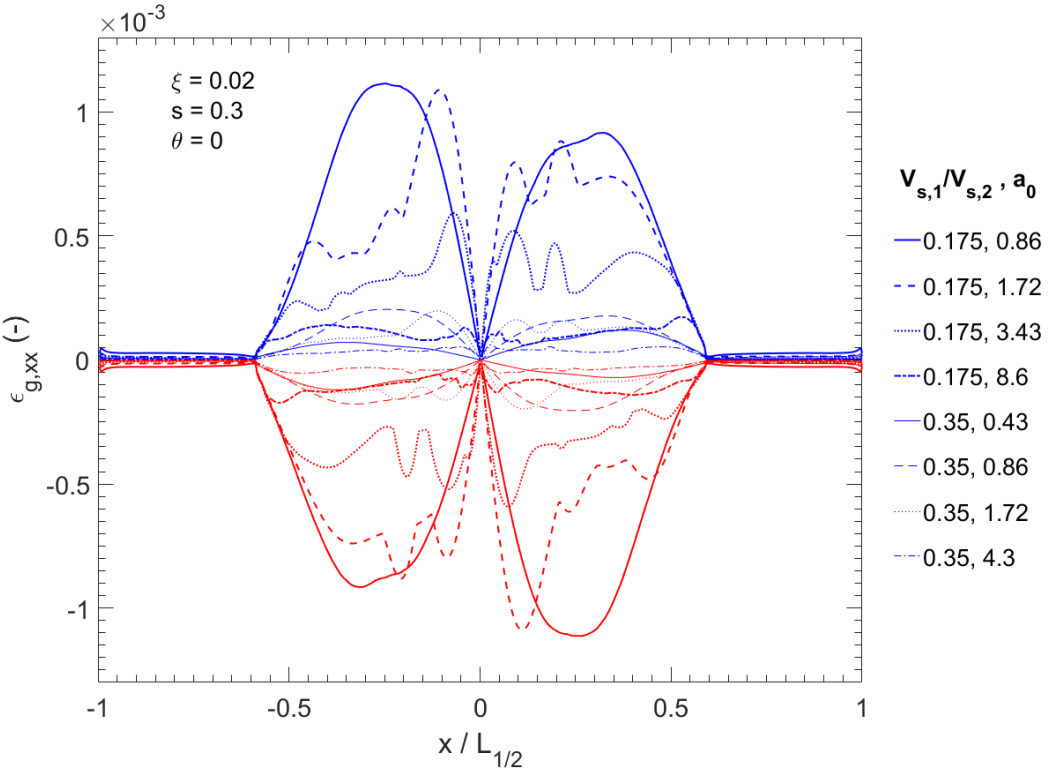

Figure 10. Envelopes of peak tensile (positive) and compressive (negative) axial ground strains along the surface for different scenario 2 cases.

In Figure 11, seismogram synthetics of the horizontal accelerations at the surface of the sites are plotted for typical high-frequency input excitations with $\theta = 0$. It can be seen in Figure 11a for scenario 1 that

the coherent input excitation at the bedrock level generates highly non-synchronous ground motions at the surface associated with large axial strains. A clearer picture of the wave patterns for scenario 1 is provided in Figure 12, where contours of the shear and vertical normal strain fields are displayed at different times. As can be seen in the top left figure, the wave front forms an oblique transition zone in the vicinity of the inhomogeneity boundary due to the different propagation velocities in the soft and firm soils. Mode conversion occurs inside the transition zone generating a P-wave that travels upwards and gives the so-called 'parasitic' vertical motion component at the surface. Apparent in the softer deposit are the successive reflections of the oblique SV- and P-wave fronts at the surface and the bedrock interface. Notably, both the large axial strains and the parasitic vertical component are not captured by the standard, Newmark-type, approach adopted in most relevant codes of practice, including ALA.

The situation for scenario 2 as pictured in Figure 11b is more complex. Upon the first arrival of the wave at the sloping interface, mode conversion produces SV- and P-waves. The refracted rays arrive at the surface and interfere with the vertically impinging rays arriving from the valley center (focusing effect). Further mode conversion of the oblique wave fronts occurs at the surface and subsequently at the valley-rock interface, resulting in trapping of the waves inside the valley and clearly longer response duration. More importantly, Rayleigh waves (marked with red lines) are generated at the edges of the valley, which travel back and forth along its surface with estimated velocities of 120 and 67 m/sec. The symmetry of the domain results in maximum motion amplification at the valley center due to constructive interference of the R-waves.

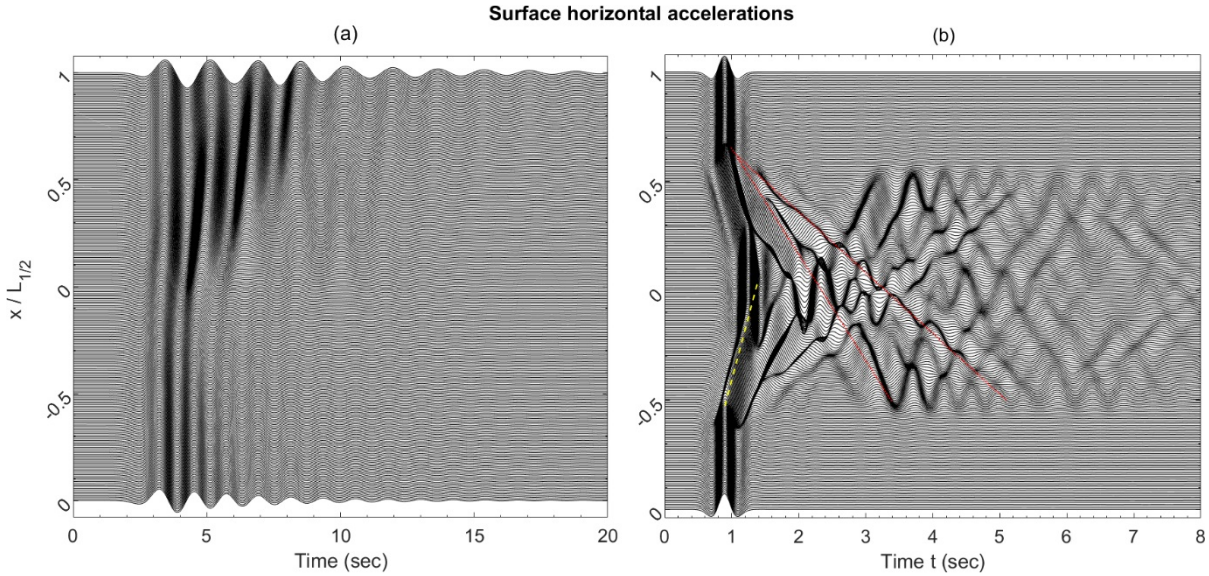

Figure 11. 2D synthetics of surface horizontal acceleration for (a) scenario 1 with $f = 5\,Hz$, $\theta = 0$ and (b) scenario 2 with $f = 5\,Hz$, $\theta = 0$. The red line in (b) marks the refracted wave front along the dipping interface, while the red lines indicate the *R*-waves generated at the valley edges.

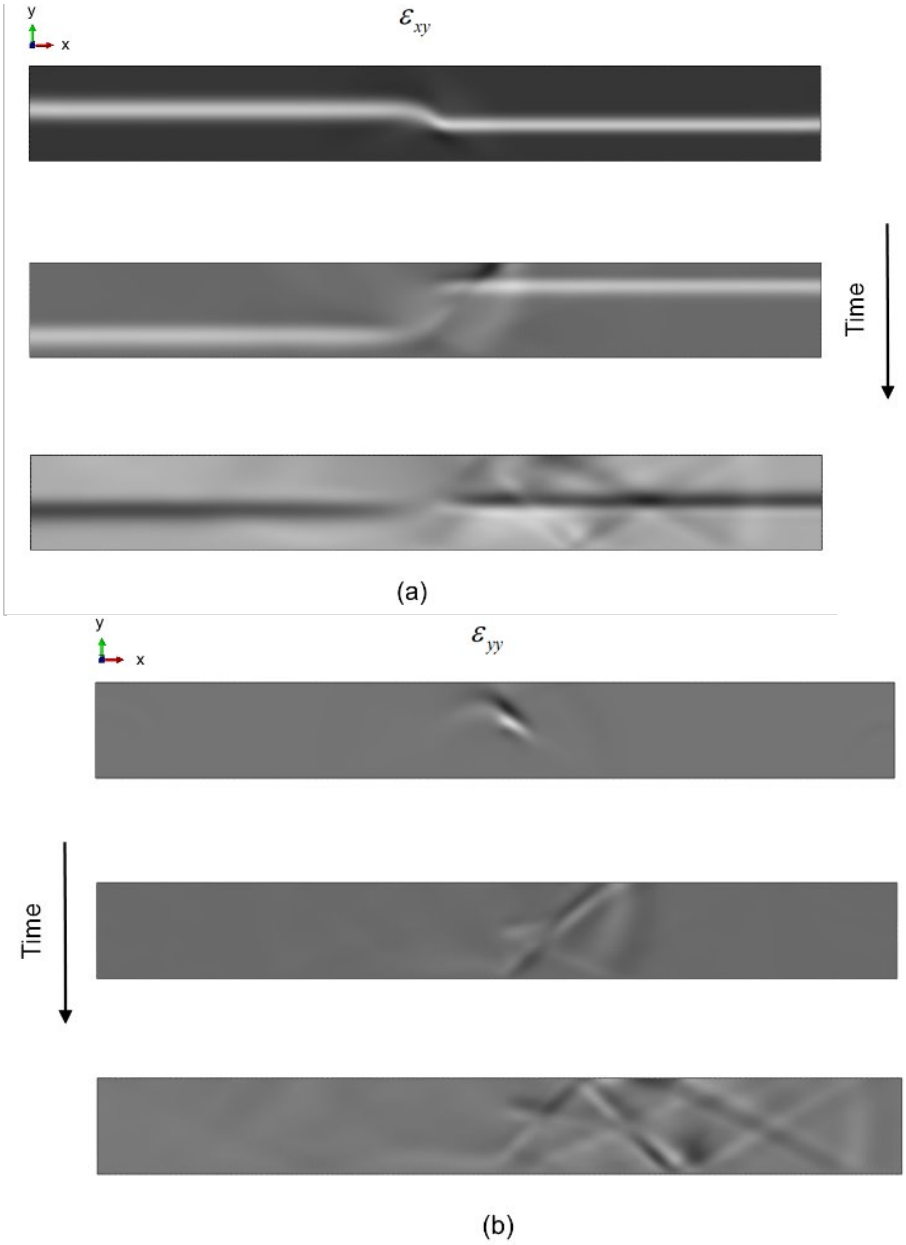

Figure 12. Snapshots of the complete (a) shear strain field (SV-waves) and (b) vertical normal strain field (P-waves) in a typical scenario 1 site subject to a vertically incident 5 Hz Ricker pulse. Discernible are the upward travelling inclined wave fronts at the vertical boundary and the ensuing successive reflections at the surface and the bedrock boundary. The parasitic vertical component of motion is evidenced in (b).

Figure 13 presents the time evolution of the elastic ground axial strains at the surface for a scenario 1 case with $H = 60$ m, $V_{s,1} = 140$ m/sec, $\ell_t / H = 0.16$, $\theta = 0$ and $\xi = 0.02$. As expected, the out-of-phase horizontal motions of the two deposits generate alternating tensile-compressive strain near the vertical boundary, and more towards the softer of the two deposits. The strains attain their peaks early with the first direct pulse arrival and then decay with time. In Figure 14, the instantaneous horizontal distributions of the axial strains and horizontal displacements at an assumed pipeline depth of 1 m from the surface, corresponding to the timeframe of the maximum compressive strain, are plotted for the most unfavorable cases of the two scenarios examined. Although the strain magnitudes appear quite similar,

the produced distributions are different: a pipeline buried in a scenario 1 site would primarily suffer from axial compression at the critical timeframe, while the same pipeline buried in a scenario 2 site would be subjected to both compression and tension along close-by segments.

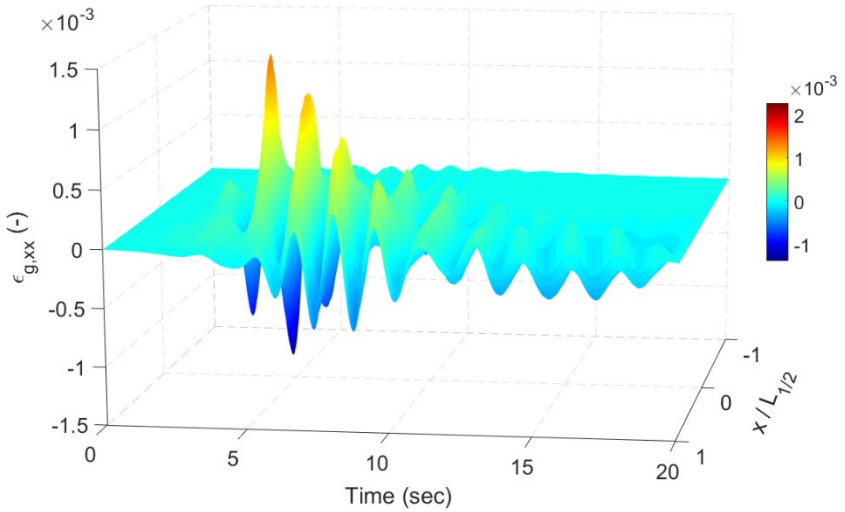

Figure 13. Time-variation of ground axial strain field at the surface of a model with $H = 60$ m, $V_{s,1} = 140$ m/sec, $\ell_t / H = 0.16$, $\theta = 0$ and $\xi = 0.02$.

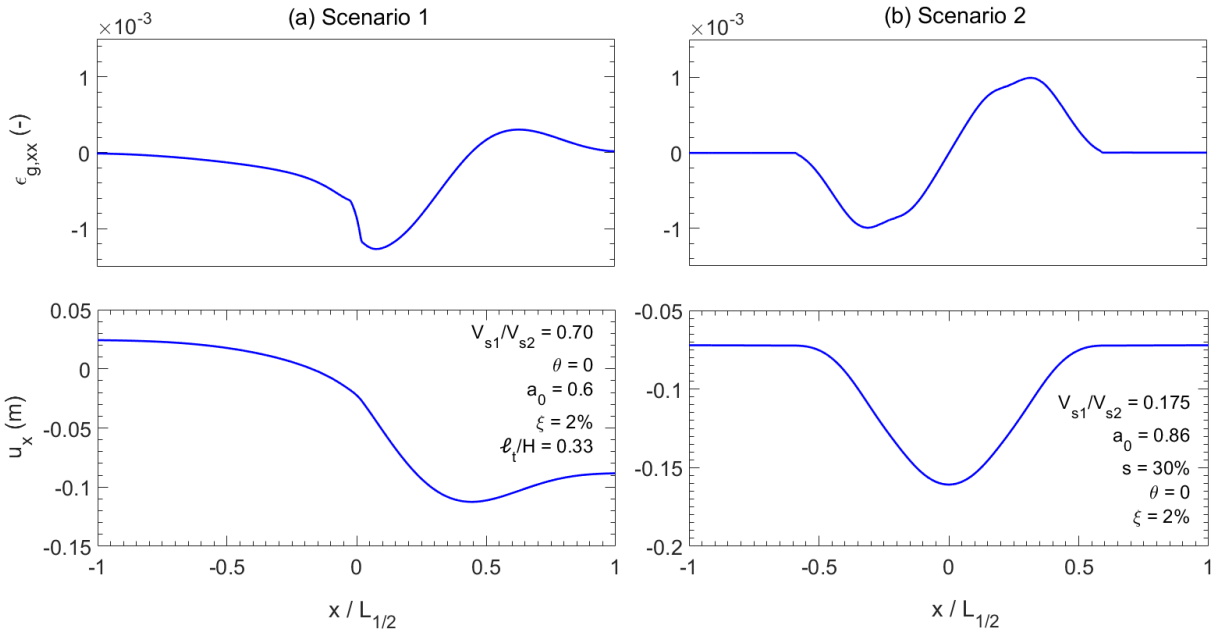

Figure 14. Critical spatial profiles of axial ground strain and horizontal ground displacement for (a) scenario 1 and (b) scenario 2.

Effect of exciting frequency

The effect of the frequency content of the seismic excitation on the peak strains was studied and was found to be major. Low frequency vibrations produce consistently larger peak axial strains, regardless of soil impedance ratio r_v and viscous damping ratio ξ as illustrated throughout Figure 15. This is accentuated by the fact that *PGA* -scaling of the input motions is used, thus naturally integration of high-

frequency acceleration histories will produce lower amplitude displacements. But one cannot deduce definite conclusions because motion amplification depends not only on the excitation frequency, but also on the natural frequencies of the site. Thus, it can be said that for the primarily soft soil deposits examined herein, it comes as no surprise that low frequency excitations tend to induce larger motions and deformations.

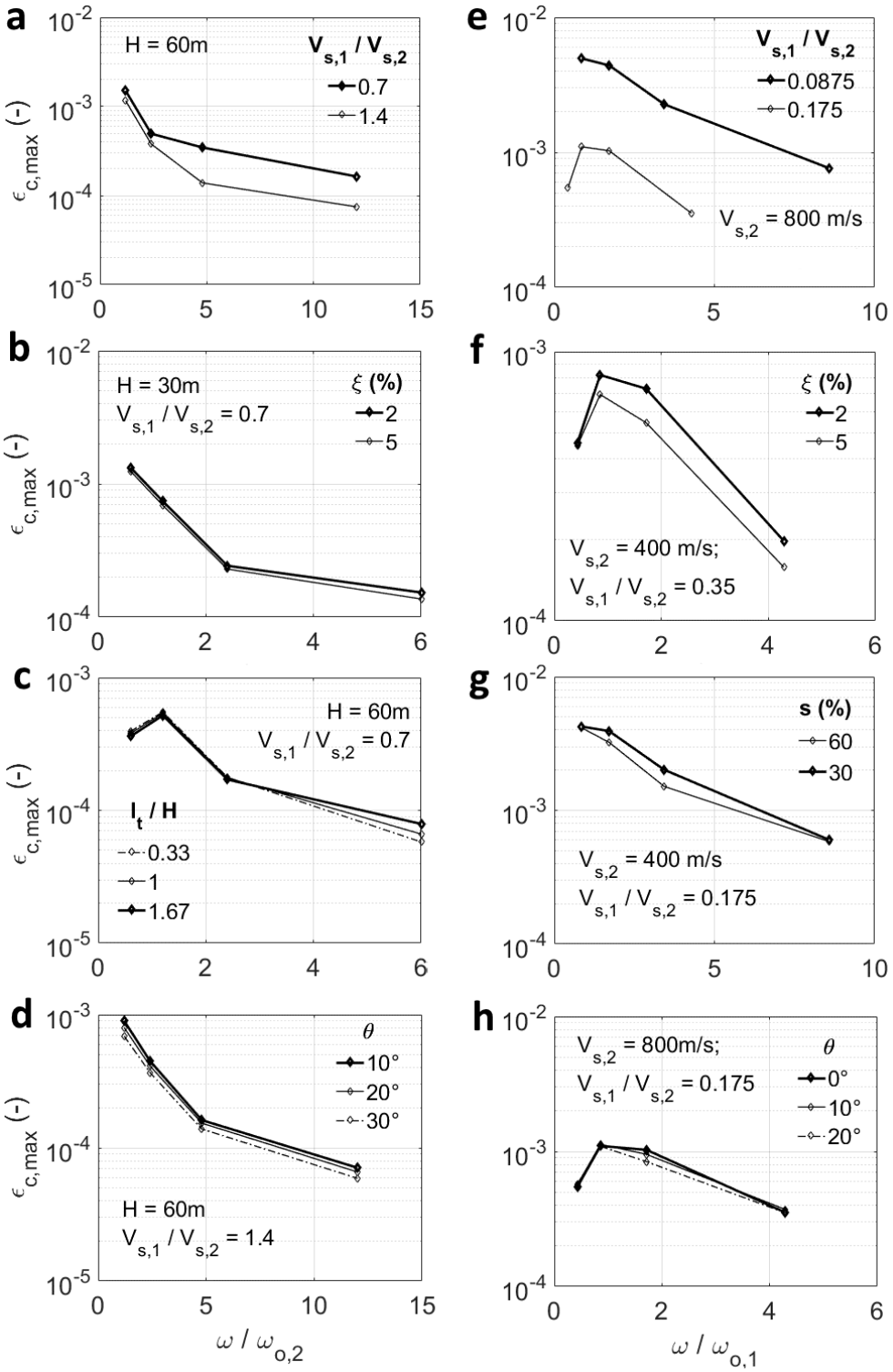

Figure 15. Variation of peak compressive axial ground strains with normalized excitation frequency for different soil impedance ratios (a and e), viscous damping ratios (b and f), transition zone lengths for Scenario 1

(c), valley slopes for Scenario 2 (g), and wave incidence angles (d and h). Where not mentioned, reference parameters are implied as follows: for Scenario 1, $\xi = 2\%$, $\theta = 0$, $\ell_t / H = 0.33$; for Scenario 2, $\xi = 2\%$, $\theta = 0$, $s = 30\%$.

Effect of site impedance ratio

In accord with common sense, the site impedance ratio proves to be a defining factor of the level of the induced ground axial strains in both sites. The larger the impedance ratio, the larger the axial strain at the interface (Figure 15a and e). However, it is not only the relative stiffness of the site that controls the strain magnitudes, but also the absolute elastic stiffness. This was inferred from the fact that sites with same velocity contrasts but different absolute velocity values sustain different levels of axial strains. Overall, softer sites of the type 1 or 2 develop larger normal strains than stiffer ones with similar velocity contrasts under the same bedrock excitation. Figure 15a demonstrates this fact: a scenario 1 site with deposit velocities 70 and 100 m/sec develops 1.36 to 2.14 times larger normal strains than a site with deposit velocities 140 and 100 m/sec, the two sites having roughly the same velocity contrast (1/0.7 = 1.43 ≈ 1.4).

Effect of the spatial rate of change of stiffness (scenario 1)

For scenario 1, the impact of the extent of the transition zone between the two deposits was investigated. Introducing the length of the transition zone of $G_{\max}$ as a parameter and varying $G_{\max}$ in a linear fashion had imperceptible effect on the computed strains compared to the case of abrupt transition, as clearly depicted in Figure 15c. For this reason, all equivalent-linear models in the following employ a discontinuous transition to simplify the modelling process.

Effect of boundary slope (scenario 2)

Steeper basins give lower strain peaks for an intermediate range of wavelengths, because a larger part of the wave energy is reflected initially back to the half-space at the inclined rock-valley interface (see Figure 15g). On the other hand, strain magnitudes appear insensitive to the boundary slope for higher frequency excitations.

Effect of wave incidence angle

An obliquely impinging wavefront seems to have a somewhat obscure effect on the axial strains, depending on whether the wave passage contribution is in or out of phase with the primary local site effects, but is generally minor for both site scenarios (Figure 15d and h). The increase in strains is at most one order of magnitude smaller than the ones attributed to inhomogeneities and this can be verified using exact solutions for homogeneous soils [4]. An explanation particular to the sites considered is also that, when the seismic waves strike under angle, part of the oncoming energy in scenario 1 sites is reflected back from the inhomogeneity boundary, depending on the impedance contrast of the bordering deposits, or, in the case of scenario 2 sites, always a smaller amount of energy is transmitted to the valley compared to the vertical incidence case.

3.5.2 Nonlinear response (strong input motion)

By conducting a short parametric study using equivalent-linear site response models, we were able to identify the parameters leading to the most critical load on the pipeline when excitations are strong. Figure 16 plots the ground axial strain synthetics on the surface of the two scenarios for the typical case of Ricker pulse excitation. Clearly, for scenario1, the strain distribution along the surface appears more localized towards the location of the boundary, with large positive and negative peaks reaching 2.1% and -1.3%. For scenario 2, it is observed that the strong nonlinear soil response suppresses the scattering-induced strain peaks above the wedge toes seen in case of elastic soil response, and 'drags' them towards the sharp valley-rock boundary, with peak magnitudes comparable to those of scenario 1.

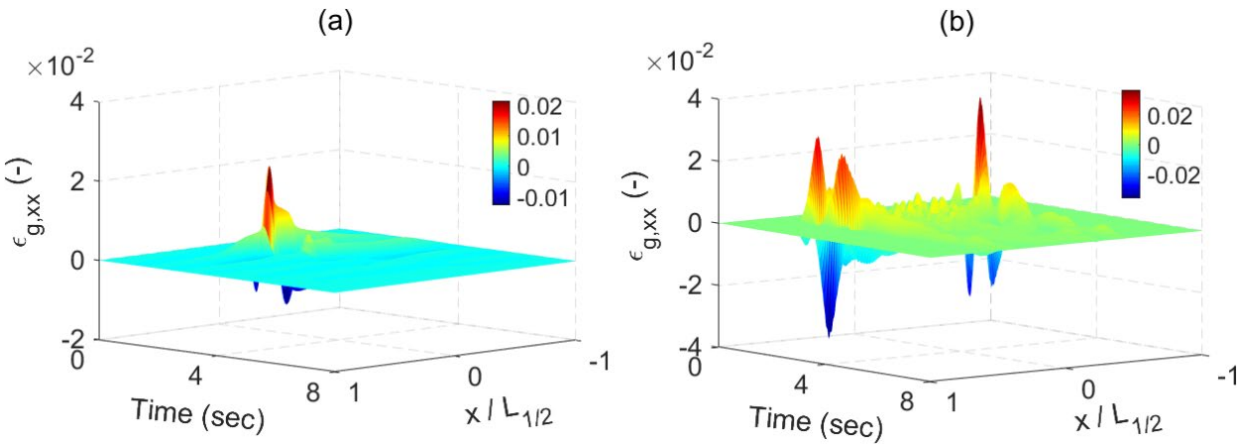

Figure 16. Time-variation of ground axial strain field at the surface for cases (a) S1NL7 and (b) S2NL6.

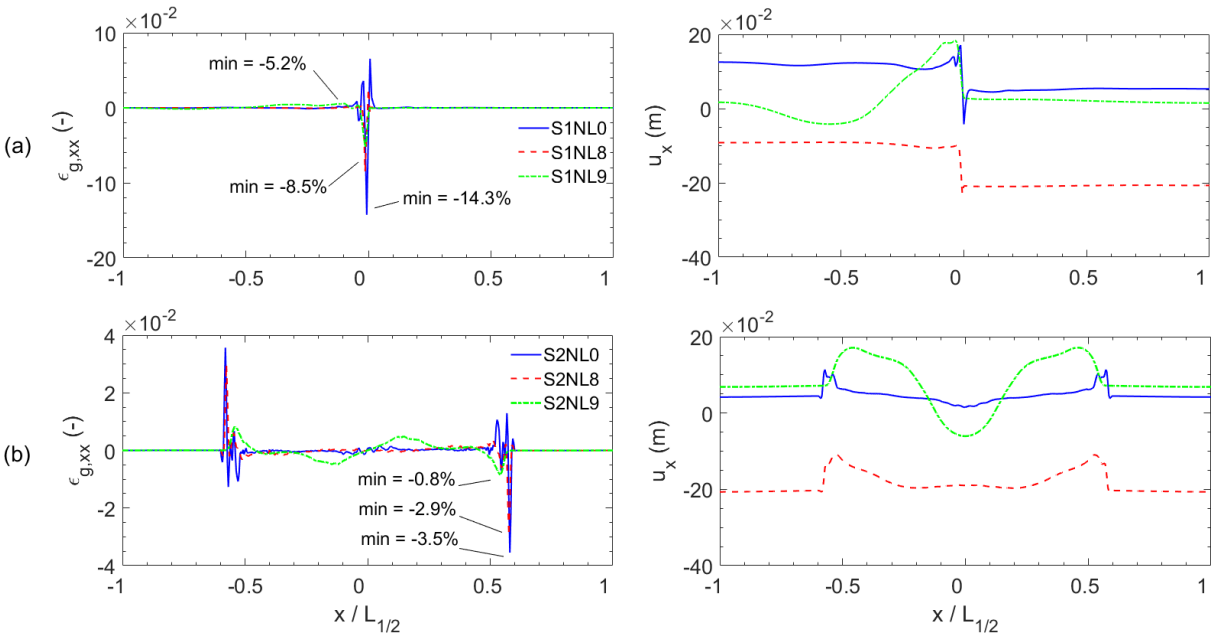

Figure 17. Spatial profiles of axial ground strain and horizontal ground displacements for all real earthquake excitations for (a) scenario 1 and (b) scenario 2.

Figure 17 presents the critical strain and displacement distributions for the two scenarios for all real earthquake input motions; the peak compressive strains are displayed as well. It is seen that, for scenario 1, the critical spatial profile of the horizontal soil displacement occurs when the horizontal vibrations of the two adjacent soil deposits are nearly out of phase, as manifested by the step-like form of the profile. At this time instant, a sharp axial strain spike develops almost right at the boundary, as shown in the top left subplot. This behaviour is a direct consequence of the degradation of G with increasing γ_c, given that the Young's modulus degradation is assumed proportional to that of G. At the converged iteration of the analysis, an average maximum shear strain of roughly 0.3% and 0.04% develops at pipeline depth of the soft and stiff deposit, resulting in a ten-fold and two-fold *G*-modulus reduction, respectively.

The deformation pattern in the soil is not as simple for scenario 2; a state of anti-symmetry is apparent in the strain profile shape with respect to the valley center, meaning that a sharp compressive strain peak develops at one valley edge concurrently with a sharp tensile strain peak of roughly equal magnitude at the other valley edge. For both scenarios, the most unfavourable soil demand is found for the input motion with the lowest mean period T_m (Imperial Valley) and for the largest site impedance contrast; strains appear to decay with increasing T_m. Notably, the results are sensitive to the type and number of *G*-γ-*D* curves employed in the model.

4 Nonlinear soil-pipe interaction analysis

In this section, we illustrate some modelling aspects as well as the prominent features of the shell response. Results for two analysis cases from scenario 1 are presented: one for linear elastic soil response under weak excitation and one for nonlinear soil response under strong excitation. The same pipeline model is used in both cases. The analyses were undertaken in Abaqus.

4.1 Modelling aspects

The differential horizontal soil motions extracted from the critical time frame of the ground response history are imposed as displacement boundary conditions on the trench soil body. These displacements are kept constant with the vertical coordinate over the soil domain, on the grounds that the depth of the simulated domain is small compared to the maximum predominant wavelength of the impinging waves examined ($3D_o/\lambda_{o,\max} < 0.10$), hence, the in-plane motion of the soil particles does not vary much in depth. This assumption has been checked against using vertically varying motion. Note that, in this study, although the full two-dimensional soil seismic response is computed, only its dominant axial component is applied on the pipeline.

The loading sequence is as follows: first, gravity load is applied to compute the in-situ stress state and to ensure that interface friction is 'activated'; the internal pressure is also applied in this initial loading step. Then, large-deformation quasi-static stress analysis of the near-field soil-pipe system is performed

for the imposed soil displacements. Geometry perturbation is also introduced in the mesh to trace the load-deflection path post-buckling using a built-in Riks algorithm.

4.1.1 Geometrical and mechanical properties of the pipeline

An actual NG pipeline was simulated, namely the Transitgas pipeline crossing Switzerland; relevant data was retrieved from the owner company website [55] (Table 6). A typical cross-section of the near-field soil-pipeline system is sketched in Figure 18a, where the dashed lines indicate the truncation of the half-plane. Plastic behavior is considered for the pipeline steel [56] through classical J_2-flow plasticity and a von Mises yield criterion. A Ramberg-Osgood curve with a 'yield offset' of 0.5% and a hardening exponent n = 11 was fitted to a bilinear isotropic curve describing the uniaxial tensile behaviour of the material (Figure 18b). The soil medium is modelled in this phase as secant elastic, with its strain-compatible modulus obtained from the equivalent-linear site response analysis in Stage 1.

Table 6. Geometrical and material properties of the simulated NG pipeline [55].

Pipeline	R (mm)	t (mm)	R/t	σ_y (MPa)	P/P_o (*)	Burial depth to crown (mm)	ε_u (%)
TransitGas	450	12	37.5	448	0.62	1000 (assumed)	4

(*) $P_o = \sigma_y t / R$ is the yield pressure.

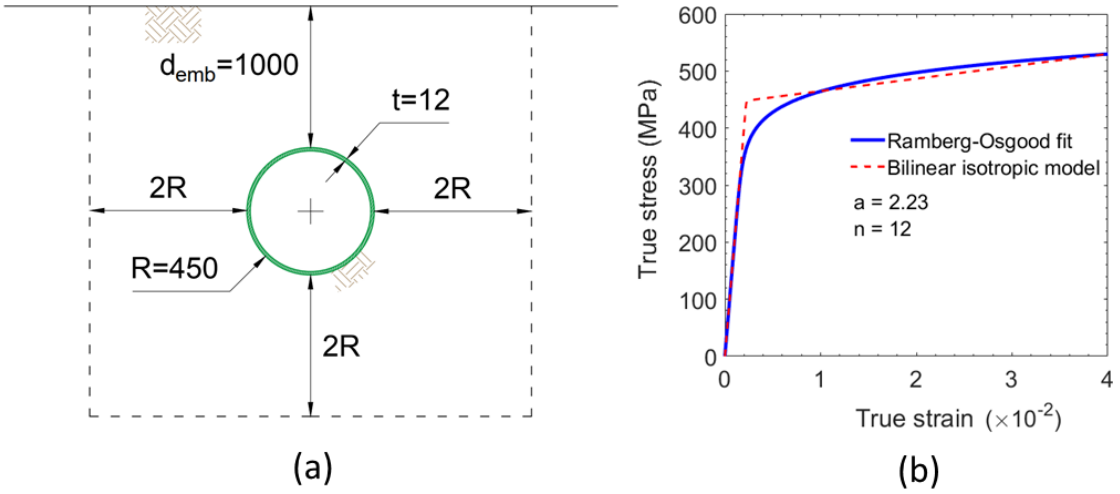

Figure 18. (a) The truncated cross-section of the soil-pipeline system used in our model (units in mm); (b) uniaxial tensile stress-strain response of API X65 steel (n = hardening exponent, a = yield offset × E/σ_y).

4.1.2 Pipe shell and soil discretization

The reduced integration S4R finite strain shell element having both membrane and bending stiffness is selected from the Abaqus element library to discretize the pipe. Within the critical deformation zone, that is, around the soil inhomogeneity boundary, the discretization is made fine enough to adequately resolve the inelastic buckling modes of an axially compressed unconstrained cylindrical steel shell. The elastic axial half-wavelength of such a shell with E = 200 GPa and ν = 0.3 in uniform axial compression

is $\lambda_{c,el} \approx 1.72\sqrt{Rt}$ [57]. However, buckling in the post-elastic range is associated with shorter half-wavelengths which can be approximated by the following expression [57]:

$$\lambda_{c,p} \approx \lambda_{c,el} \sqrt[4]{E_p / E} \tag{6}$$

In order to achieve the necessary mesh resolution in the examined case, a plastic modulus $E_p = 0.1E$ is assumed giving a $\lambda_{c,p}$ that is roughly 50% of the elastic one and an element length $\ell_{el} = 1$ cm is found sufficient for this purpose. Note that, in the presence of internal pressure, the wavelength of the wrinkles is longer than in the case of pure axial compression. Away from the critical zone, the mesh is made progressively less dense as the axial dimension of the pipe shell elements is increased up to 1m to contain the computational cost. Besides, in these regions, strain amplitudes are very small and the pipeline is not expected to exhibit any radial deflections. An aspect of the pipeline mesh used is given in Figure 20a. Linear hexahedral (brick) elements are used to discretize the soil domain.

4.1.3 Interface contact

Initially, the soil cavity and the external pipeline walls are in full contact. Standard Coulomb friction is chosen to describe the relative tangential motions which can be arbitrarily large, while loss of contact in the normal direction (detachment) is allowed at the same time. More realistic empirical models for axial SPI have been recently reported in the literature [58] that account for soil dilatancy effects and post-peak soil resistance decay, but are not adopted herein. The surface-to-surface contact discretization option is used in the Abaqus environment, which in this case ensures coupling between the tangential and normal components of relative motion.

According to O'Rourke and El Hmadi [37], the interface friction coefficient for buried steel pipelines can be calculated as $\mu = (0.5 \div 0.9)\tan\varphi$, where φ is the soil angle of shearing resistance. For sands, it is typically $\varphi = 29^\circ \sim 41^\circ$, thus a lower and upper bound $\mu_{\min} = 0.28$ and $\mu_{\max} = 0.78$ can be established. Sheil *et al*. [59] also infer a value range 0.55 ~ 0.6 from cyclic loading tests. The maximum of the previous values $\mu = 0.78$ is conservatively selected for the present model for identifying an upper bound of the soil-to-pipe strain transmission.

4.1.4 Boundary conditions

If we consider the two limiting cases of a pipeline clamped at its ends and a pipeline completely unrestrained, we choose to be on the conservative side and leave the pipeline ends free to move horizontally. This decision is driven by the belief that, away from any lateral ground heterogeneities, a pipeline is expected to move with the soil under vertically incident in-plane shear waves. In reality, there is a degree of axial restraint imposed at the pipeline ends, which could be better captured by incorporating nonlinear end springs to account for the pipeline continuity (see [60]). Standard static boundary conditions have been applied to the bounding soil surfaces.

4.1.5 Initial geometric imperfections

A local, stress-free, biased axisymmetric imperfection is introduced [1], which is merely a standard sinusoid modulated by a second sinusoid to produce a peak amplitude at the middle section of the pipeline. The radial deflection function is computed by Eq. (7), where positive values are assumed in the outward direction from the mid-surface. The peak amplitude is taken as $w_0 + w_1 = 0.13t$. The imperfection pattern is applied over a short critical pipeline zone with $L_{crit} = 4$ m, centered at the site vertical border (see Figure 20b).

$$\bar{w}(x) = \left[w_0 + w_1 \cos\left(\frac{\pi x}{N\lambda_c} \right) \right] \cos\left(\frac{\pi x}{\lambda_c} \right), \quad -L_{crit}/2 \le x \le L_{crit}/2 \text{ and } 2N\lambda_c = L_{crit} \tag{7}$$

The soil mesh across the contact interface is exactly matched with the pipeline mesh to prevent initial gaps during the generation of the perturbed mesh. It should be mentioned that, in reality, line pipes often come with residual stresses induced by the manufacturing process, which sometimes may be quite large. This aspect is not considered in this study.

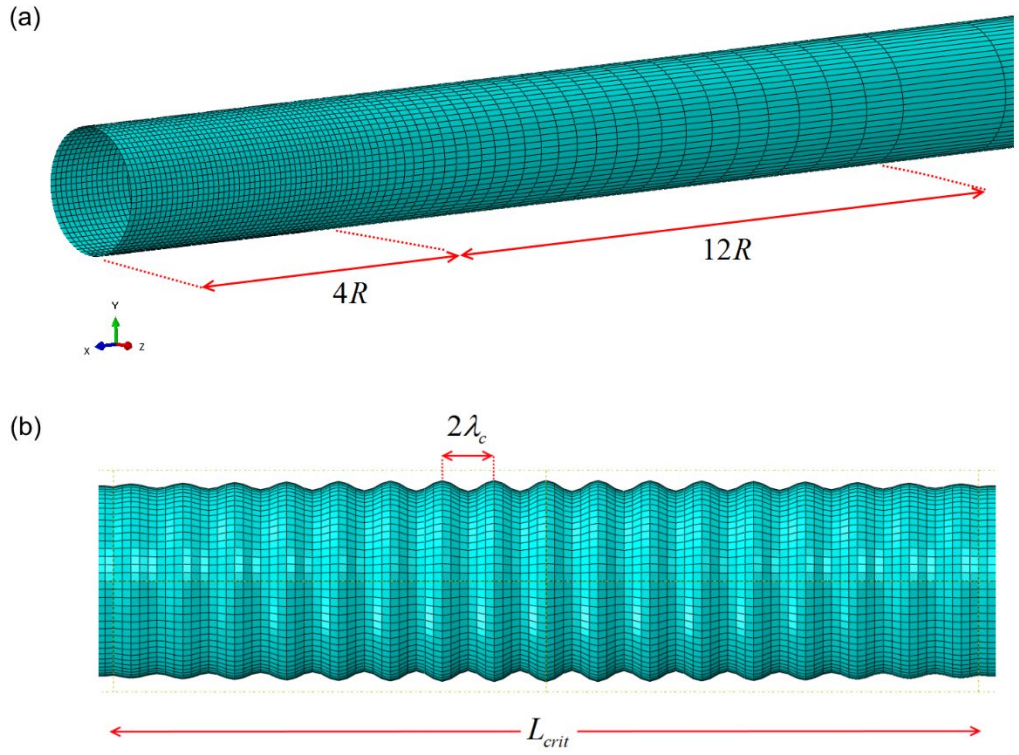

Figure 19. (a) Perspective of the progressively refined pipeline mesh towards the mid-section at the left end; (b) close-up view of the biased axisymmetric imperfection shape used (radial displacements exaggerated).

4.2 Pipeline response to weak input ground motion

In stage (2), the critical displacement pattern from case S1NL0 (Figure 18a) is applied on the brick soil elements. A contour plot of the Mises stresses over the whole pipeline is provided in Figure 20. The

maximum demand-to-capacity ratio in terms of Mises stresses, where the capacity is defined as the steel yield limit, was found to be 0.45, indicating that the pipeline responds in the linear elastic regime. Figure 21 depicts how elastic axial strain varies along the pipeline. Over the cross-section, it remains nearly uniform. It can be seen that the peak pipeline strain is almost 10 times smaller than that of the ground, which reveals that the pipe body is in a sliding state. Generally, the amount of shaking generated due to low-intensity input motions produces relatively small axial ground strains ($<1.5\times10^{-3}$), which are unlikely to lead the pipeline response above the yield limit, at least for the scenarios examined here. The induced stress in the pipe is by no means negligible, but it comes largely from the internal pressure and not seismic shaking. It is noted that the pipeline retains its contact with the soil (no separation).

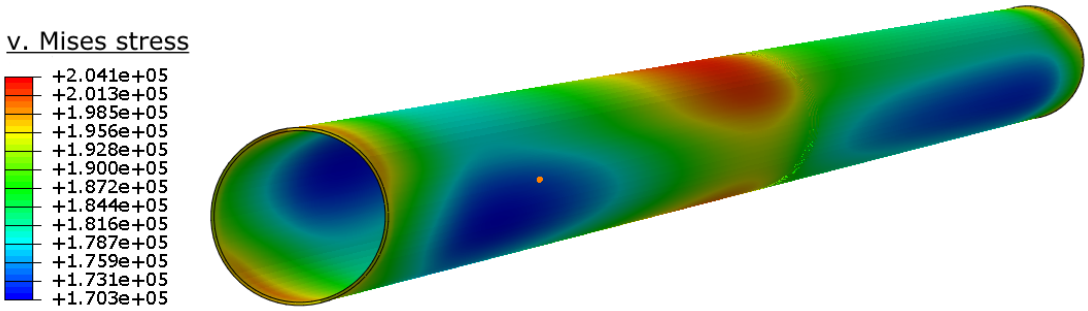

Figure 20. Von Mises stress contours on the pipeline due to the critical ground excitation.

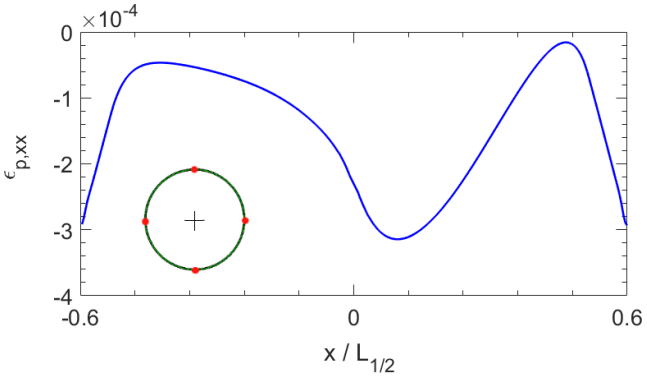

Figure 21. Axial strain pattern along the pipeline for the critical weak ground excitation. The ordinate plots strain values averaged over four integration points across the pipe section (red dots).

4.3 Pipeline response to strong input ground motion

This time, the soil demand from critical case S1NL1 is imposed on the soil-pipeline system. The larger and more localized axial ground strains produce a different response pattern on the pipeline. The distribution of the average axial strain along the pipeline is shown in Figure 22. Clearly, the distribution is qualitatively similar to that of the surrounding soil, as a sharp peak appears near the mid-section. The noise in the critical zone is due to the wrinkling pattern that develops with increasing load.

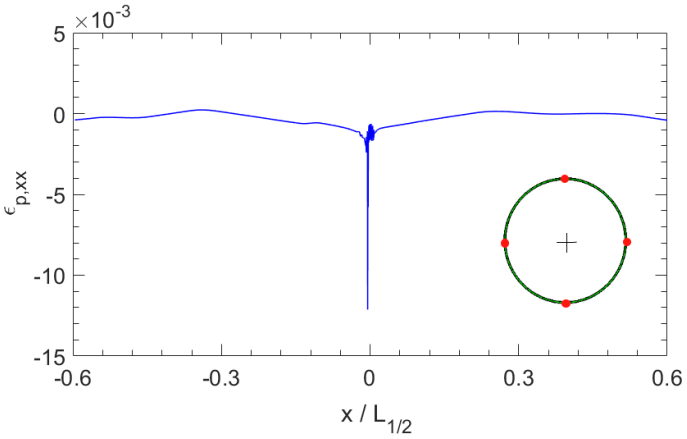

Figure 22. Axial strain pattern along the pipeline for the critical strong excitation. The ordinate plots strain values averaged over four integration points across the pipe section (red dots).

In addition to the rigid body motion, a complex state of stress is present locally in the pipeline as a result of axial load-bending moment interaction. Figure 23 presents the axial force-displacement response (compression negative) and the bending moment-axial curvature response of the pipeline. The kinematic quantities plotted on the abscissas are the average axial shortening (δ_x/ℓ_{cr}) and the dimensionless mean axial curvature of the shell cross-section ($\overline{\kappa}/\kappa_o$). The averaging takes place inside a critical zone ℓ_{cr} defined by the reference sections in Figure 24, because this is where the localization of deformation occurs. The integrated axial force and bending moment are computed at the critical (control) section, 0.96 m apart from the mid-section. Following Corona and Kyriakides [61], the normalizing quantities are taken as follows: $P_o = 2\pi Rt\sigma_y$, $M_o = \sigma_y \mathrm{D}_o^2 t$, $\kappa_o = t/D_o^2$, where $D_o = D - t$. Analysis has continued beyond the target load magnitude, until collapse is reached, so as to examine the overall response characteristics of the buried shell.

The succession of events in the pipeline state is described now and is illustrated in Figure 24. Due to the reduced uplift resistance of the cover soil compared to that of the bed soil, increasing compression triggers *P-δ* effects in the vertical plane. A bending moment starts to develop along with the axial force in the pipeline very close to the point of maximum ground strain causing a slight localized uplift of the pipeline and the cover soil, and a simultaneous change in diameter ΔD is detected ① (ovalization). The first wrinkles (marked with ∧) appear shortly before the onset of yield (marked with ▼) inside the region of large axial strains. Their strongly non-axisymmetric shape suggests that they are dominated by bending. The amplitudes of the wrinkles grow and, soon after, a moment maximum is attained; wrinkles then gradually localize around two regions: principally, the invert (compression) of the mid-section, and secondarily the crown of a section at a distance of roughly $2R$ ②. Next, the moment drops and a limit axial load is reached (marked with ×). The axial rigidity becomes negative, a characteristic of shells in the post-critical regime, and the pipe buckles locally at the invert. The buckle is quite sharp

and, though not the scope of this study, it is conjectured that it may lead to wall tearing and loss of containment with further stress concentration.

For comparison purposes, included in Figure 23a is also the axial stress-strain response of the same pipeline in a radially infinite medium (i.e., no surface relief) with equivalent properties. The induced bending moment in this case is negligible and the pipe responds essentially in pure axial compression, displaying a collapse load 26% larger than the shallow-buried one. The buckling pattern caused by the surface relief in our case is in contrast to the typical axisymmetric or non-axisymmetric modes encountered in unconstrained or uniformly constrained shells. It is confirmed that combined axial compression and flexure effectively leads to localized collapse in the form of a downward facing, outward-protruding bulge, at lower axial loads than the ones predicted for pure axial compression under uniform radial constraint, as outlined in Ref. [31].

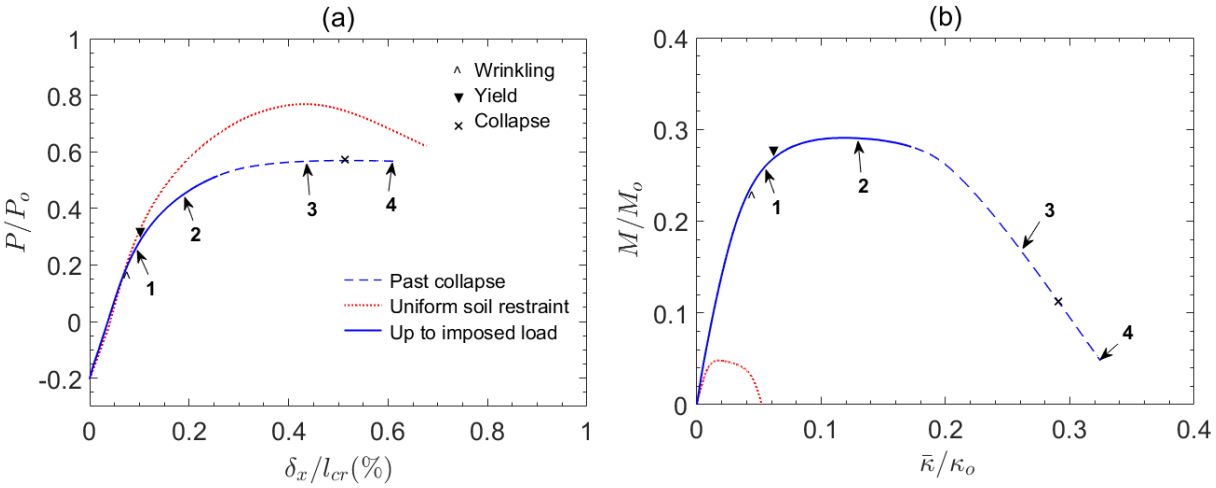

Figure 23. (a) Average axial load - displacement response and (b) average bending moment - axial curvature response of the pipeline shell in the critical zone ℓ_{cr} due to the critical strong input motion. Numbers and shapes on the paths identify events of interest visualized in Figure 24.

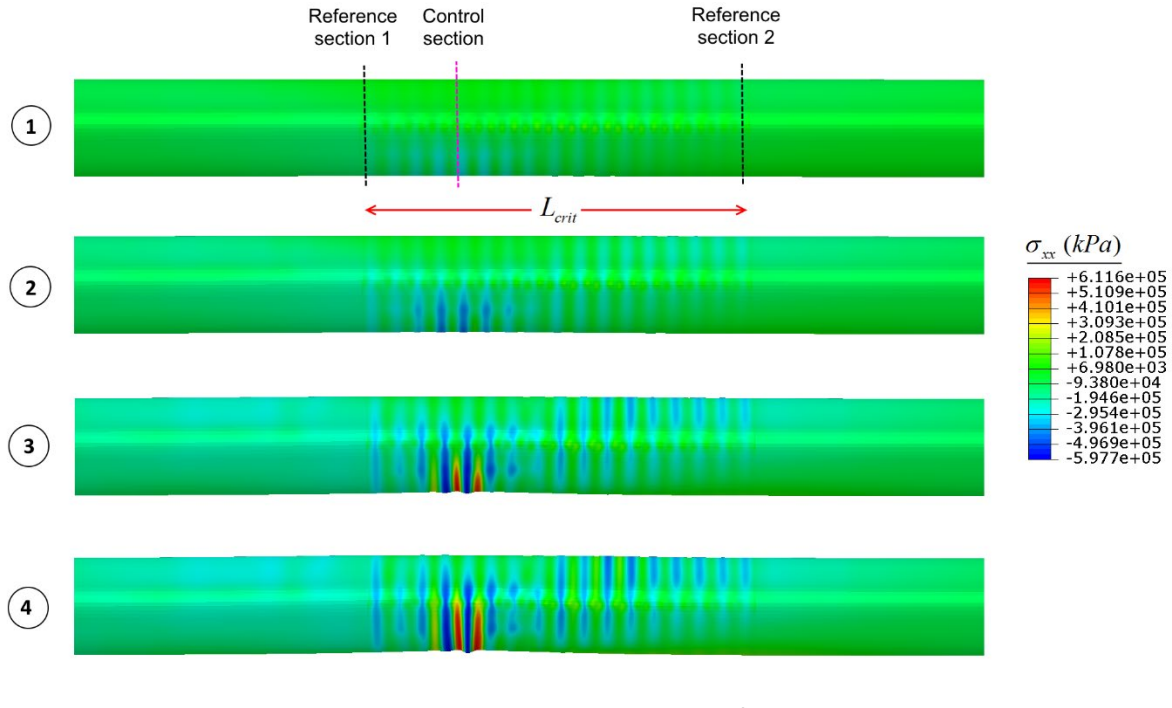

Figure 24. Successive phases of deformation of the pipeline due to axial compression-bending interaction; σ_{xx} contours overlaid.

Figures 25 and 26 offer some understanding into the evolution of the contact state at the soil-pipe interface with increasing axial soil straining. Figure 25 shows the longitudinal profile of axial slip and contact opening along the crown and bottom lines. It is evident that considerable relative axial displacements occur within an extended zone with a length of roughly $100R$ centered at the boundary. Outside this zone, slippage values are found to be much smaller, revealing that the frictional strength is not exhausted. This huge difference demonstrates the strongly local character of the problem. The same can be said for the normal relative displacements, but in this case the gaps that develop are contained in a shorter zone coinciding with the imperfection zone. Not unreasonably, the gaps are more pronounced on the bottom side of the section due to the uplift motion of the pipeline and the incipient separation. Where gaps are present, the axial interaction is not defined, hence zero axial slip values are plotted in Figure 25a. Initially, the pipeline and the soil are perfectly bonded and no relative motion occurs. Slippage initiates just outside the imperfection zone and spreads outwards, while the separation zone grows mildly. Figure 26 plots frictional shear stress against relative displacement in the longitudinal sense at different positions along the pipeline and over the cross-section. It can be seen that, at the same longitudinal position, different axial soil-pipe interaction responses hold for different locations over the circumference, with points near the bottom displaying larger interface resistance and stiffness and hardening behavior due to the increased soil pressures (Figure 26, right). The axial soil-pipe interaction appears different very close to the vertical inhomogeneity border (Figure 26, left) as the notably

increased soil pressures lead to a striking increase in the interface shear strength. At the bottom, the shear stress drops to zero because a gap opens there.

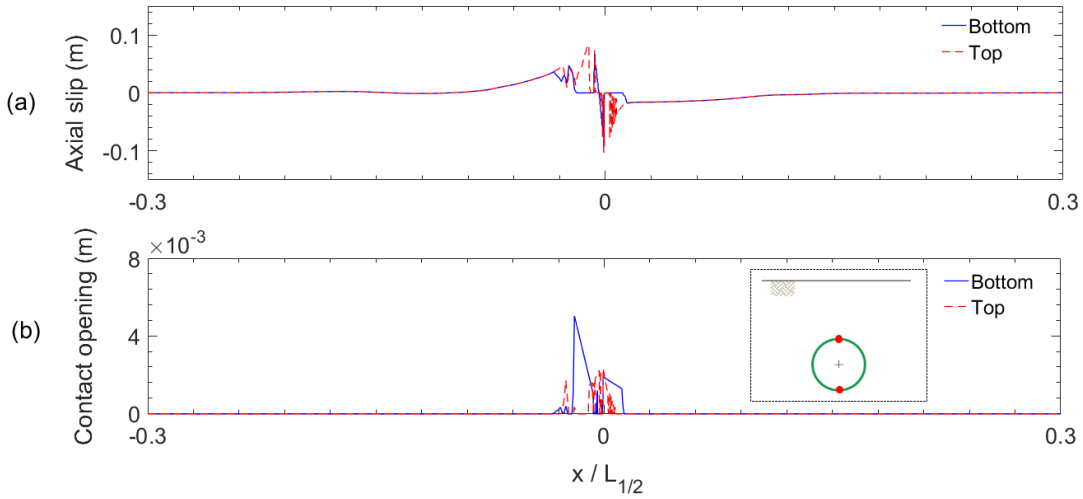

Figure 25. Distribution of (a) axial and (b) normal relative soil-pipe displacements along the top and bottom line of points of the pipeline.

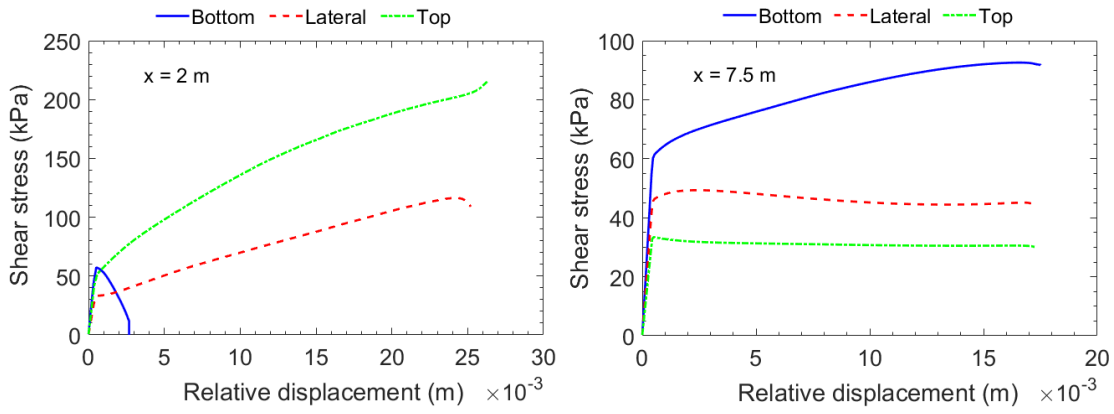

Figure 26. Contact shear stress – displacement at the soil-pipe interface evaluated at different points over the cross-section and length of the pipeline.

5 Discussion and conclusions

This paper seeks to provide by numerical means a well-founded answer to the question whether a buried, steel-made, transmission natural gas pipeline can experience shell-type buckling under earthquake ground shaking, and examine the contributing factors to its emergence. The focus is restricted to unfavorable but naturally occurring cases in which the pipeline crosses soil formations with irregular conditions and the ground excitation arises as plane SV-waves. Based on the assumption that inertial and kinematic SPI is negligible, a sub-structured, decoupled numerical analysis methodology is proposed, where the complete soil-pipeline system is successively analyzed as (i) a ‘global’ plane

ground response model and (ii) a 'local' 3D continuum-shell assemblage with contact explicitly modeled. The methodology is applied to study the linear and nonlinear local site effects on the earthquake response of the pipeline. The key findings are summarized below:

1. *Linear soil response*: In scenario 1 sites, characterized by a lateral ramp transition zone of soil stiffness, the peak compressive axial ground strains develop in the softer soil deposit, very close to the vertical border, with values ranging from 0.01% to 0.15%. Wave mode conversion occurs inside the transition zone from the soft to the stiffer deposit, generating a *P*-wave that travels upwards and produces considerable vertical motions at the surface. Therefore, the critical load profile for a pipeline buried in a scenario 1 site would consist of a combination of out-of-phase horizontal soil displacements and a localized vertical displacement inside the transition zone.

   In scenario 2, valley-type, sites, the anti-symmetric axial strain field at the surface is dominated by local wave scattering inside the valley, predominantly Rayleigh waves generated at the valley edges. The absolute peaks occur above the wedge toes in a range between 0.01% and 0.11%. A pipeline buried in such a site would be subjected simultaneously to compression and tension along the two opposite segments.

   The peak axial ground strain values depend mainly on the impedance contrast of the soil deposits and the resonant frequencies that amplify oscillations. The absolute stiffness of the deposits is also influential, as the softer soils analyzed herein experienced larger deformations. The worst-case soil deformations are obtained for a combination of large impedance ratios, soft soil deposits and long-period input motions. In contrast, the additional strains due to the wave passage effect are much smaller than the ones due to local site effects. Geometric parameters examined such as the transition zone length in scenario 1 and the boundary slope in scenario 2 are shown to also have minor influence.
2. *Nonlinear soil response*: It is shown that when considering nonlinearity in the cyclic soil behavior under higher intensity motions, the induced axial ground strains can be as much as two orders of magnitude larger (~ 15%) compared to linear elastic response, a difference attributed to the sharp decrease of the *G*-modulus with increasing cyclic shear strain. The strain profiles also tend to be more localized towards the border of the two soil deposits for scenario 1, giving a sharp peak. The displacement load pattern could be approximated with certain functional forms, such as a logistic or step function, to facilitate parametric pipeline buckling analyses. For scenario 2, wave scattering effects are suppressed by the nonlinearity of the soil response and strain peaks are shifted towards the inclined rock-valley interface, with magnitudes comparable to scenario 1. The severity of these strains poses potentially greater risk to underground structures.
3. *Pipeline response*: The answer to the central question of this study as posed in its title is that, under certain circumstances, a typical buried, large-diameter, high-pressure steel NG pipeline subject to seismic wave propagation loading can indeed exhibit non-axisymmetric shell wrinkling that will

progressively localize with load increase and cause collapse. These circumstances include *SV*-waves propagating through sharply changing soil profiles in the pipeline direction and producing strong asynchronous ground motions. It was found that pipeline deformation attributable to elastic axial ground strains caused by weak exciting pulses of PGA = 0.05g is negligible, with peak Mises stresses not exceeding 50% of the yield limit of API X65 steel. However, it is shown that soil nonlinearity bears crucial influence on the induced pipeline deformation, causing section-averaged axial pipe strains as large as 1.2%. A unique state of deformation is observed in a confined pipe segment not longer than 4 diameters, close to the location of peak ground strain, which is described by marked interaction between shell- and beam-mode buckling modes. As demonstrated, the bending moment developing in the pipe as a result of the surface relief reduces its critical axial buckling load by 26% compared to its uniformly confined counterpart, and leads to collapse upon formation of a sharp fold on the invert of the pipe. The contact state can be highly non-uniform both over the length and the depth of the pipeline: extensive slippage and loss of contact occurs within the large soil deformation zone, but perfect bond conditions prevail in a distance from it.

The preceding analysis demonstrates that inelastic buckling instabilities when a shallow-buried transmission NG pipeline is loaded axially in compression by transient differential ground displacements should be a consideration for design. No provisions exist in the present seismic codes of practice that address this complex behavior. The outcomes of this study may lay the ground for further investigations of the sensitivity of the buckling capacity of buried pressurized pipelines under similar loading to various problem parameters. Furthermore, it is hoped that the presented analysis methodology for capturing earthquake-induced buckling phenomena will serve as a benchmark for design and assessment applications where a compromise between sophistication and computational demand is sought.

6 Acknowledgements

This work was financially supported by the Horizon 2020 Programme of the European Commission through grant MSCA-RISE-2015-691213-EXCHANGE-Risk (Experimental & Computational Hybrid Assessment of NG Pipelines Exposed to Seismic Risk, www.exchange-risk.eu). The first author also expresses his gratitude to the Engineering and Physical Sciences Research Council for financially supporting his doctoral studies (grant no.: EP/M507994/1).

References

[1] Kyriakides S, Corona E. Plastic Buckling and Collapse Under Axial Compression. Mech. Offshore Pipelines Buckling Collapse, Vol. I, 2007, p. 280–318. doi:http://dx.doi.org/10.1016/B978-008046732-0/50011-8.

[2] Lee LNH, Ariman T, Chen CC. Elastic-plastic buckling of buried pipelines by seismic excitation. Int J Soil Dyn Earthq Eng 1984;3:168–73. doi:10.1016/0261-7277(84)90032-9.

[3] Newmark NM. Problems in wave propagation in soil and rock. Proc. Int. Symp. wave Propag. Dyn. Prop. earth Mater., Albuquerque: University of New Mexico Press; 1968, p. 7–26.

[4] St John CM, Zahrah TF. Aseismic design of underground structures. Tunn Undergr Sp Technol 1987;2:165–97. doi:10.1016/0886-7798(87)90011-3.
[5] Zhang B, Papageorgiou AS. Simulation of the response of the marina district Basin, San Francisco, California, to the 1989 Loma Prieta earthquake. Bull Seismol Soc Am 1996;86:1382–400.
[6] Assimaki D, Kausel E, Gazetas G. Wave propagation and soil-structure interaction on a cliff crest during the 1999 Athens Earthquake. Soil Dyn Earthq Eng 2005;25:513–27. doi:10.1016/j.soildyn.2004.11.031.
[7] Psarropoulos PN, Tazoh T, Gazetas G, Apostolou M. Linear and Nonlinear Valley Amplification Effects of Seismic Ground Motion. Soils Found Japanese Geotech Soc 2007;47:857–71.
[8] Gelagoti F, Kourkoulis R, Anastasopoulos I, Tazoh T, Gazetas G. Seismic wave propagation in a very soft alluvial valley: Sensitivity to ground-motion details and soil nonlinearity, and generation of a parasitic vertical component. Bull Seismol Soc Am 2010;100:3035–54. doi:10.1785/0120100002.
[9] Scandella L, Paolucci R. Earthquake induced ground strains in the presence of strong lateral soil heterogeneities. Bull Earthq Eng 2010;8:1527–46. doi:10.1007/s10518-010-9186-6.
[10] O'Rourke TD, Palmer MC. Earthquake performance of gas transmission pipelines. Earthq Spectra 1996;12:493–527.
[11] Chen WW, Shih B, Chen Y-C, Hung J-H, Hwang HH. Seismic response of natural gas and water pipelines in the Ji-Ji earthquake. Soil Dyn Earthq Eng 2002;22:1209–14. doi:10.1016/S0267-7261(02)00149-5.
[12] Sakurai A, Takanashi T. Dynamic Stresses of Underground Pipelines During Earthquakes. Proceed. 4th World Conf. Earthq. Engng., Santiago, Chile: 1969, p. 81.
[13] Housner GW, Jenningst PC. The san fernando california earthquake 1972;1:5–31. doi:10.1002/eqe.4290010103.
[14] Benfer NA, Coffman JL. San Fernando, California Earthquake of Feb. 9, 1971. Washington DC: 1974.
[15] Hall JF, Holmes WT, Somers P, Institute EER. Northridge earthquake of January 17, 1994: reconnaissance report. Earthquake Engineering Research Institute; 1996.
[16] EQE Summary Report. The January 17, 1995 Kobe Earthquake. 1995.
[17] O'Rourke MJ. Wave Propagation Damage to Continuous Pipe. Tech. Counc. Lifeline Earthq. Eng. Conf. (TCLEE), Oakland, CA, June 28-July 1., Reston, VA: American Society of Civil Engineers; 2009. doi:10.1061/41050(357)76.
[18] Esposito S, Giovinazzi S, Elefante L, Iervolino I. Performance of the L ' Aquila (central Italy) gas distribution network in the 2009 (M w 6 . 3) earthquake 2013;2009:2447–66. doi:10.1007/s10518-013-9478-8.
[19] O'Rourke MJ, Liu X. Response of Buried Pipelines Subject to Earthquake Effects. 1999.
[20] Hindy A, Novak M. Earthquake response of underground pipelines. Earthq Eng Struct Dymamics 1979;7:451–76.
[21] Nishio N, Ukaji T, Tsukamoto K. Experimental Studies and Observation of Pipeline Behavior During Earthquakes. PVP-Vol. 43, 1980, p. 67–76.
[22] Nishio N, Ishita O, Tsukamoto K. Model experiments on the behavior of buried pipelines during earthquakes. Am. Soc. Mech. Eng., Press. Vessel. Pip. Div., (Tech. Rep.) PVP; (United States), vol. PVP-VOL. 7, 1983.
[23] Akiyoshi T, Fuchida K. Seismic Resposne of Pipeline Systems Buried in Dipping Soil Layers. Proc. 9th World Conf. Earthq. Eng., Tokyo-Kyoto, Japan: 1988.
[24] Liu X, O'Rourke MJ. Seismic Ground Strain at Sites With Variable Subsurface Conditions. In: Yuan JX, editor. Comput. Methods Adv. Geomech., Wuhan: A. A. Balkema; n.d., p. 2239–44.
[25] Ando H, Sato S, Takagi N. Seismic Observation of a Pipeline Buried at the Heterogeneous Ground. Proc Tenth World Conf Earthq Eng 1992:5563–7.
[26] Liang J. Dynamic Response of Pipelines Laid Through Riverbeds. PVP-Vol. 312, 1995, p. 147–152.
[27] Liang J. 3-D Seismic Response of Pipelines Through Multiple Soil Media. PVP-Vol. 312, 1995, p. 101–107.
[28] Zerva A, Ang A.-S, Wen YK. A Study of Seismic Ground Motion for Lifeline Response Analysis. Civ Eng Stud Struct Res Ser (University Illinois Urbana-Champaign, Dep Civ Eng 1985.
[29] Zerva A. Lifeline response to spatially variable ground motions. Earthq Engineeirng Struct Dyn 1988;16.
[30] Chen CC, Ariman T, Lee LHN. Buckling Analysis of Buried Pipelines Under Seismic Loads. Proc. 7th Eur. Conf. Earthq. Engng, 1980, p. 249–256.
[31] Yun H, Kyriakides S. On the beam and shell modes of buckling of buried pipelines. Soil Dyn Earthq Eng 1990;9:179–93. doi:10.1016/S0267-7261(05)80009-0.
[32] Psyrras NK, Sextos AG. Safety of buried steel natural gas pipelines under earthquake-induced ground shaking : a review. Soil Dyn Earthq Eng 2017;106:254–77. doi:10.1016/j.soildyn.2017.12.020.
[33] Mavridis G. A, Pitilakis KD. Axial and transverse seismic analysis of buried pipelines. Elev. World

Conf. Earthq. Eng., 1996.
[34] Makra K, Chavez-Garcia FJ. Site effects in 3D basins using 1D and 2D models: an evaluation of the differences based on simulations of the seismic response of Euroseistest. Bull Earthq Eng 2016;14:1177–94. doi:10.1007/s10518-015-9862-7.
[35] Kubo K. Behavior of Underground Water pipes During an Earthquake. Proc. 5th World Conf. Earthq. Eng., Rome: 1974, p. 569–78.
[36] Shinozuka M, Koike T. Estimation of Structural Strains in Underground Lifeline Pipes. 1979.
[37] O'Rourke MJ, Hmadi K El. Analysis of continuous buried pipelines for seismic wave effects. Earthq Eng Struct Dyn 1988;16:917–29. doi:10.1002/eqe.4290160611.
[38] Papadopoulos SP, Sextos AG, Kwon O-S, Gerasimidis S, Deodatis G. Impact of spatial variability of earthquake ground motion on seismic demand to natural gas transmission pipelines. 16th World Conf. Earthq. Eng. Santiago, Chile, 9-13 January., 2017.
[39] Psyrras N, Sextos AG, Kwon O-S, Gerasimidis S. Safety factors of buried steel natural gas pipelines under spatially variable earthquake ground motion. 11th Natl. Conf. Earthq. Eng., Los Angeles, California: Earthquake Engineering Research Institute; 2018. doi:10.1016/j.soildyn.2017.12.020.
[40] Vucetic M, Dobry R. Effect of Soil Plasticity on Cyclic Response. J Geotech Eng 1991;117:89–107. doi:10.1061/(ASCE)0733-9410(1991)117:1(89).
[41] Vucetic M. Cyclic Threshold Shear Strains in Soils. J Geotech Eng 1994;120:2208–28. doi:10.1061/(ASCE)0733-9410(1994)120:12(2208).
[42] Kaklamanos J, Baise LG, Thompson EM, Dorfmann L. Comparison of 1D linear, equivalent-linear, and nonlinear site response models at six KiK-net validation sites. Soil Dyn Earthq Eng 2015;69:207–19. doi:10.1016/j.soildyn.2014.10.016.
[43] Kramer SL. Geotechnical earthquake engineering. Upper Saddle River: Upper Saddle River. : Prentice Hall; 1996.
[44] Abaqus Documentation. 6.14. Providence, RI: Dassault Systèmes; 2014.
[45] McKenna F, Fenves GL, Scott MH. Open System for Earthquake Engineering Simulation. PACIFIC Earthq Eng Res Cent 2000.
[46] Seed HB, Idriss IM. Soil moduli and damping factors for dynamic response analyses. Berkeley, Calif. : College of Engineering, University of California; 1970.
[47] Darendeli MB. Development of a new family of normalized modulus reduction and material damping curves 2001.
[48] Hudson M, Idriss I, Beikae M. QUAD4M: a computer program to evaluate the seismic response of soil structures using finite element procedures and incorporating a compliant base. Cent Geotech Model Dep Civ Environ Eng Univ California, Davis, CA 1994.
[49] Ishibashi I, Zhang X. Unified Dynamic Shear Moduli And Damping Ratios of Sand and Clay. Soils Found Japanese Geotech Soc 1993;14:369–75. doi:10.1248/cpb.37.3229.
[50] Zhang J, Andrus RD, Juang CH. Normalized Shear Modulus and Material Damping Ratio Relationships. J Geotech Geoenvironmental Eng 2005;131:453–64. doi:10.1061/(ASCE)1090-0241(2005)131:4(453).
[51] Lysmer J, Kuhlemeyer R. Finite dynamic model for infinite media. J Eng Mech Div 1969;95:859–877.
[52] Ricker N. Further developments in the wavelet theory of seismogram structure. Bull Seismol Soc Am 1943;33:197–228.
[53] Rathje EM, Abrahamson NA, Bray JD. Simplified frequency content estimates of earthquake ground motions. J Geotech Geoenvironmental Eng 1998;124:150–8. doi:10.1061/(ASCE)1090-0241(1998)124:2(150).
[54] Hashash YMA, Musgrove MI, Harmon JA, Groholski DR, Phillips CA, Park D. DEEPSOIL 6.1, User Manual 2016.
[55] Transitgas AG. The Pipeline System 2013. http://www.transitgas.org/EN/pipeline.aspx (accessed July 20, 2017).
[56] Ramberg W, Osgood WR, States. U, Aeronautics. NAC for. Description of stress-strain curves by three parameters 1943.
[57] Timoshenko SP, Gere JM. Theory of Elastic Stability. McGraw-Hill; 1961.
[58] Sarvanis GC, Karamanos SA, Vazouras P, Mecozzi E, Lucci A, Dakoulas P. Permanent earthquake-induced actions in buried pipelines: Numerical modeling and experimental verification. Earthq Eng Struct Dyn 2017:1–22. doi:10.1002/eqe.3001.
[59] Sheil BB, Martin CM, Byrne BW, Plant M, Williams K, Coyne D. Full-scale laboratory testing of a buried pipeline in sand subjected to cyclic axial displacements 2015.
[60] Vazouras P, Dakoulas P, Karamanos SA. Pipe-soil interaction and pipeline performance under strike-slip fault movements. Soil Dyn Earthq Eng 2015;72:48–65. doi:10.1016/j.soildyn.2015.01.014.
[61] Corona E, Kyriakides S. On the collapse of inelastic tubes under combined bending and pressure. Int J Solids Struct 1988;24:505–35. doi:10.1016/0020-7683(88)90005-4.